SARS-CoV-2 ORF3a blocks lysosomal cholesterol egress by disrupting VPS39-regulated NPC2 trafficking and BMP metabolism

Baley A. Goodson[1], Valeria Montenegro Vazquez[1], Aliza Doyle[1], Oralia M. Kolaczkowski[1], Rui Liu[2], Jingyue Jia[3], Morié Ishida[4], Hu Wang[5], Xianlin Han[5], Chunyan Ye[3], Alison M. Kell[1], Steven B. Bradfute[3], Monica Rosas Lemus[1], Jing Pu[1,*]

[1]Department of Molecular Genetics and Microbiology, University of New Mexico Health Sciences Center, Albuquerque, NM, USA.

[2]Department of Pharmaceutical Sciences, College of Pharmacy, University of New Mexico Health Sciences Center, Albuquerque, NM, USA.

[3]Department of Internal Medicine, University of New Mexico Health Sciences Center, Albuquerque, NM, USA.

[4]Neurosciences and Cellular and Structural Biology Division, Eunice Kennedy Shriver National Institute of Child Health and Human Development, National Institutes of Health, Bethesda, MD, USA.

[5]Department of Medicine, UT Health San Antonio Long School of Medicine, San Antonio, TX, USA.

*Correspondence: jpu@salud.unm.edu; T: 505-272-8890

Run title: ORF3a blocks lysosomal cholesterol via NPC2 and BMP pathways

Abstract

Cholesterol homeostasis relies on lysosomes, which release free cholesterol from degraded lipids. We show that SARS-CoV-2 blocks lysosomal cholesterol export through its protein ORF3a. ORF3a binds the HOPS subunit VPS39, and disrupting this interaction restores cholesterol trafficking. Two mechanisms underlie this defect. First, ORF3a–VPS39 interaction traps the sorting receptor CI-MPR and the retrieval complex retromer in endosomes/lysosomes, impairing trafficking of the cholesterol transporter NPC2. Retromer deletion reproduced these defects. Second, ORF3a reduces bis(monoacylglycerol)phosphates (BMPs), lysosomal lipids required for cholesterol export. Lipidomics and proteomics revealed altered metabolism of BMP precursors, mitochondrial phosphatidylglycerols (PGs), and reduced mitochondrial proteins at lysosomes. ORF3a–VPS39 interaction decreased lysosome–mitochondrion membrane contact sites (MCS), excluding autophagy or mitochondrion-derived vesicles as routes for PG transfer. VPS39 deletion decreased the MCS and BMPs. These findings identify VPS39 as a regulator of NPC2 trafficking and BMP biosynthesis and reveal that ORF3a disrupts both pathways to block cholesterol egress.

Key words:

Cellular cholesterol transport, HOPS, retromer, bis(monoacylglycerol)phosphates (BMPs), lysosome-mitochondrion interactions.

INTRODUCTION

Cholesterol plays a vital role in maintaining cellular structure and functions. Thus, cells tightly regulate cholesterol levels and distribution through multiple pathways. Cholesterol pathways are not only disturbed in metabolic disorders but also hijacked in infectious diseases. COVID-19, caused by the SARS-CoV-2 virus, has been associated with significant disruptions in cholesterol metabolism[1–5]. In cases of long COVID, an increased risk of dyslipidemia and cardiovascular diseases is marked by elevated low-density lipoprotein (LDL) cholesterol and reduced high-density lipoprotein (HDL) cholesterol levels[4,5].

Lysosomes, the degradation organelles, receive and break down internalized lipoprotein particles and cellular macrolipids delivered via endocytosis and autophagy, respectively, releasing free cholesterol in the process[6]. The released cholesterol is then distributed to other cellular compartments to support structural and metabolic demands[7,8]. The cholesterol delivered to the endoplasmic reticulum (ER) serves as a signal to regulate the expression of genes that control cholesterol synthesis and uptake[9]. The cholesterol supplied to the plasma membrane is the major source for maintaining the local cholesterol pool that modulate plasma membrane fluidity and stability[10]. SARS-CoV-2 exploits plasma membrane cholesterol to enhance infectivity[11], as evidenced by a reduced binding between the viral spike protein and its host receptor after plasma membrane cholesterol depletion[12]. Therefore, the lysosomal cholesterol transport is central to cellular cholesterol homeostasis and may also play a role in SARS-CoV-2 infection.

Lysosomal cholesterol egress is the first step of cholesterol distribution. This process is primarily mediated by the lysosomal transmembrane cholesterol transporter Niemann-Pick C1 (NPC1) and the lumenal cholesterol-binding protein Niemann-Pick C2 (NPC2), which act cooperatively to transfer cholesterol out of lysosomes[8]. Additional lysosomal proteins, including the lumenal saposins and membrane proteins LAMP2[13,14], also contribute to cholesterol egress[8]. The proper trafficking and localization of newly synthesized lysosome transmembrane proteins depend on sorting signals and clathrin coats[15]. In contrast, the lysosome lumenal proteins are directed by sorting receptors, such as the mannose-6-phosphate receptors (M6PRs)[15]. These receptors deliver lysosome lumenal proteins from the trans-Golgi network (TGN) to endosomes and are subsequently recycled back to the TGN. This recycling requires retromer complexes at endosomes and lysosomes[16–19] and Golgi-associated retrograde

protein (GARP) complex at the TGN[20]. Disruption of these transport pathways by impairing M6PR, HOPS or GARP functions compromises the delivery of newly synthesized proteins to lysosomes and results in accumulation of cholesterol[18,21,22]. Such lysosomal cholesterol sequestration profoundly disrupts lipid homeostasis and impairs cell functions, a defining feature of Niemann-Pick disease type C, caused by mutations in NPC1 or NPC2[23,24]. Beyond genetic disorders, certain viruses exploit lysosomal cholesterol transport pathways to complete their life cycles. For instance, NPC1 is hijacked by Ebola virus for their infection[25].

In addition to protein-mediated cholesterol transport, the phospholipid bis(monoacylglycero)phosphates (BMPs, also called lysobisphosphatidic acids or LBPAs), play an important role in lysosomal cholesterol egress. BMPs are highly enriched in the late endosome and lysosome membrane, where they contribute to lysosome sorting and degradation functions[9,26–28]. BMP has also been implicated in viral infection by promoting viral fusion with late endosome membranes[29–32]. Beyond these function, BMPs directly interact with NPC2 to promote cholesterol egress in an NPC1-independent way, as supplementation with BMPs rescues cholesterol sequestration in NPC1-defecient cells but has no effect in NPC2-defecient cells[33,34]. The synthesis and turnover of BMPs depend on multiple lysosomal enzymes that convert the mitochondrial phospholipids phosphatidylglycerols (PGs) into BMPs and degrade BMPs through hydrolysis[35–39].

In this study, we show that SARS-CoV-2 infection drives cholesterol sequestration in lysosomes, primarily through the viral protein ORF3a. ORF3a binds the HOPS subunit VPS39, disrupting lysosomal lumenal protein trafficking by retaining the cation-independent mannose 6-phosphate receptor (CI-MPR) and retromer complex at endosomes and lysosomes. In addition, ORF3a–VPS39 interaction impairs lysosome-mitochondrion membrane contact sites, potentially limiting lipid transport from mitochondria to lysosomes required for BMP synthesis. By simultaneously disturbing these two VPS39-dependent pathways, ORF3a effectively sequesters cholesterol within lysosomes, revealing a mechanistic link between SARS-CoV-2 infection and lysosomal lipid dysregulation.

RESULTS

Increased lysosomal cholesterol in SARS-CoV-2-infected cells

To examine how SARS-CoV-2 infection alters host cholesterol at cellular levels, we infected human lung carcinoma epithelial cells A549, stably expressing the viral entry receptor ACE2 of human species (A549-hACE2), with the Washington strain of SARS-CoV-2. We confirmed infection in approximately 80% of cells by immunostaining for double-stranded RNA (dsRNA) (Figs. 1A & S1A). Using filipin staining to detect free cholesterol, we observed a marked increase in filipin signal in infected cells, appearing as punctate structures, compared to mock-treated cells (Fig. 1A). Similar observations were made in a different ACE2-overexpressing A549 cell line (Fig. S1B). Co-staining with an antibody against late endosomal and lysosomal membrane protein LAMP1 revealed that the filipin puncta colocalized with LAMP1-positive vesicles (Fig. 1A), indicating that cholesterol was sequestrated in the late endosomes and lysosomes. Due to the similarity of these two organelles, we refer them to lysosomes hereafter. Quantification of confocal images showed that lysosomal cholesterol levels significantly increased at 24- and 48-hours post-infection (Fig. 1B). Although filipin puncta were also present at 72 hours post-infection, mock cells showed elevated filipin signal, likely due to cell responses associated with high cell density[40] (Fig. 1B). Further analysis of over 1,500 infected cells using a high-content imaging system confirmed a consistent increase in filipin-positive puncta (Fig. 1C). To validate this cholesterol alteration, we infected monkey kidney cells Vero E6 with SARS-CoV-2, resulting approximately 80% infection rate (Fig. S1C). High-content imaging revealed that the infected cells displayed a significant 50–60% increase in cholesterol relative to LAMP1, compared with mock-treated cells, at 18 and 24 hours post-infection. (Figs. 1D, 1E, S1D), confirming that SARS-CoV-2 infection induces an increase in lysosomal cholesterol. This change persisted beyond the viral eclipse phase (~10 hours)[41]. Gas chromatography-mass spectrometry analysis of total cholesterol levels in mock and infected A549 cells showed no significant difference (Fig. 1F), suggesting that SARS-CoV-2 infection mainly alters cholesterol distribution within cells, possibly due to impaired lysosomal cholesterol transport.

Viral protein ORF3a is responsible for increased lysosomal cholesterol

To identify the specific viral proteins responsible for lysosomal cholesterol sequestration, we transfected A549-hACE2 cells with 28 plasmids individually, which encode SARS-CoV-2 proteins, and quantified filipin puncta 24 hours post-transfection. Most viral proteins (24 out of 28) did not show a significant effect on cholesterol distribution. NSP10 and NSP13 had modest effects, ORF10 doubled the filipin signal, and ORF3a produced the strongest increase in filipin puncta (Fig. 2A). ORF3a, expressed from a SARS-CoV-2 subgenomic RNA, is an accessory

136 protein. Unlike NSP10, NSP13, or ORF10, which were predominantly cytoplasmic (Fig. S2),
137 ORF3a displayed punctate or halo-like structures that partially co-localized with LAMP2 (Fig.
138 2B), consistent with previous reports of ORF3a localization to endosomes/lysosomes[42–44].
139 Remarkably, ORF3a-positive lysosomes appeared swollen and were filled with filipin (Fig. 1B,
140 arrow in enlarged frame 1), in contrast to ORF3a-negative lysosomes in the same cells, which
141 remained small and displayed minimal filipin signal (Fig. 1B, arrow in enlarged frame 2). This
142 suggests that ORF3a, particularly when localized on lysosomes, plays a critical role in
143 cholesterol sequestration.
144
145 To further validate this observation, we transfected HeLa cells with an ORF3a plasmid tagged
146 with a V5 epitope. ORF3a-V5 also formed punctate or halo structures, partially co-localized
147 with LAMP2, and significantly increased filipin signal (Fig. 2C,D), demonstrating that ORF3a
148 enhances lysosomal cholesterol accumulation across different cell types. Additionally, we
149 included ORF3a from SARS-CoV, which shares over 70% sequence identity with SARS-CoV-2
150 ORF3a, as a comparison. Interestingly, while SARS-CoV ORF3a also displayed a punctate
151 distribution, it did not increase filipin (Fig. 2C,D), suggesting a specificity in cholesterol
152 sequestration by SARS-CoV-2 ORF3a.
153
154 Together, these results demonstrate that SARS-CoV-2 infection sequesters host lysosomal
155 cholesterol primarily through the action of ORF3a. Expression of ORF3a alone is sufficient to
156 drive cholesterol accumulation in lysosomes, likely due to its lysosomal localization. The
157 differential effects on lysosomal cholesterol between ORF3a proteins from SARS-CoV and
158 SARS-CoV-2 may offer insights into the underlying mechanisms.
159
160 **The Structural difference between SARS-CoV and SARS-CoV-2 ORF3a**
161 Previous studies revealed that SARS-CoV-2 ORF3a, but not SARS-CoV ORF3a, interacts with
162 the host protein VPS39[42–45] (Figs. 3A & S3B), a subunit of the HOPS complex. Our recent work
163 showed that the HOPS complex is essential for lysosomal cholesterol egress, using VPS39
164 CRISPR-knockout (KO) cells[18]. SARS-CoV-2 infection did not downregulate the expression of
165 VPS39 or VPS11, another HOPS subunit (Fig. S3A). These results suggest that SARS-CoV-2
166 ORF3a disrupts lysosomal cholesterol egress by inhibiting VPS39 functions. To test this, we
167 aimed to disrupt the ORF3a-VPS39 interaction by introducing specific point mutations.
168
169 Miao et al. identified the residues S171 and W193 in SARS-CoV-2 ORF3a as crucial for its
170 interaction with VPS39, as mutating these residues to those in SARS-CoV ORF3a abolished the

171 interaction[43]. Structural analysis of SARS-CoV-2 ORF3a[46,47] revealed that W193, Y184, S171,
172 and H182 cluster near each other (Fig. 3B, upper), with W193 and Y184 forming a hydrophobic
173 surface likely involved in protein-protein interactions, while S171 and H182 are positioned
174 outside this hydrophobic surface (Fig. 3B, lower). In our alanine mutation screen, we found that
175 W193A and Y184A mutations weakened or disrupted the interaction, whereas S171A or H182A
176 mutations did not (Figs. 3C & S3C,D). This indicates that W193 and Y184, but not S171 or H182,
177 are essential for binding. Further structural analysis indicates that the hydrophobic surface
178 formed by W193 and Y184 (7.7 Å) in SARS-CoV-2 ORF3a is occluded in SARS-CoV ORF3a due
179 to a hydrogen bond between R193 and E171 (2.6 Å) and Y184 (2.8 Å), resulting a "closed
180 conformation" (Fig. 3B, upper). This model is supported by the observation that the S171E
181 mutation impairs the interaction[43], likely due to the large hydrophilic side chain of glutamic
182 acid obstructing the hydrophobic surface formed by W193 and Y184, thereby blocking the
183 interaction. Collectively, these findings suggest that W193 and Y184 form the primary binding
184 site, while S171 and H182 contribute to an optimal binding environment.
185
186 Given that both W193 and Y184 are aromatic amino acids, we hypothesized that their aromatic
187 rings play a role in the interaction. To test this, we mutated W193 to various amino acids and
188 evaluated the effects on binding. Replacing W193 with another hydrophobic aromatic amino
189 acid, such as phenylalanine, preserved the interaction. However, substituting W193 with a
190 charged aromatic amino acid, like histidine, or with a hydrophobic but non-aromatic amino
191 acid, like alanine, reduced binding. Furthermore, replacing W193 with a charged, non-aromatic
192 amino acid, such as lysine or aspartic acid, nearly abolished the interaction (Fig. 3D). These
193 results suggest that both the aromatic ring and hydrophobicity of W193 are critical for the
194 binding of SARS-CoV-2 ORF3a to VPS39.
195
196 **ORF3a-VPS39 interaction interrupts NPC2 trafficking**
197 With the understanding of structural basis of the interaction interface, we chose W193A
198 mutation to block the interaction between ORF3a and VPS39. To minimize potential artifacts
199 from overexpression, we individually introduced SARS-CoV ORF3a, SARS-CoV-2 ORF3a, the
200 SARS-CoV-2 ORF3a W193A mutant, and a linker peptide that serves as a control into HeLa-Flp-
201 In cells to generate tetracycline-inducible protein-expression cell lines. This system controls
202 protein expression levels via a pre-engineered recombination site in the cells[48,49]. Likely due to
203 low protein expression, we could not detect the ORF3a proteins by immunofluorescence (Fig.
204 S4A), but immunoblotting showed expected bands in response to induction by the tetracycline
205 analog doxycycline (Fig. 4A). Using immunoprecipitation, we confirmed that, in the Flp-In cells,

206 CoV-2 ORF3a interacted with endogenous VPS39, and the W193A mutation abolished this
207 interaction (Fig. 4B). High-content imaging quantification revealed that doxycycline-induce
208 expression of ORF3a increased filipin signaling by 50-60% compared to the control cells (Figs.
209 4C,D & S4B). Importantly, the W193A mutant significantly reduced ORF3a-induced cholesterol
210 accumulation (Figs. 4C,D & S4B), demonstrating that the ORF3a-VPS39 interaction is
211 responsible for the cholesterol defect.
212
213 Previous research has shown that ORF3a expression increases lysosome pH[42] and
214 compromises lysosomal membrane integrity[50], raising the question of whether lysosomal
215 membrane damage or dysfunction leads to cholesterol sequestration. To investigate this, we
216 permeabilized lysosomal membranes using the lysosomotropic agent Leu-Leu-O-Me (LLOMe)
217 and confirmed membrane damage with the marker galectin-3[51] (Fig. S4C). Elevated lysosomal
218 cholesterol was detected in the LLOMe treatment as well as in the treatment by lysosome
219 deacidifying reagents, such as the ionophore monensin or V-ATPase inhibitors bafilomycin and
220 chloroquine (Fig. S4D). These results showed that lysosome damage and pH increase could
221 sequestrate cholesterol. However, we did not detect galectin-3 puncta in the Flp-in cells (Fig.
222 S4E), suggesting that ORF3a does not markedly damage lysosomes in these cells, and that there
223 are other mechanisms that interrupt cholesterol independent of lysosome damage.
224
225 We next examined the lysosomal cholesterol transporters NPC proteins in the Flp-In cells.
226 Immunoblotting the endogenous proteins did not show an obvious difference in NPC protein
227 levels between the four Flp-in cell lines (Fig. S4F) or between mock and infected cells (Fig. S4G).
228 Immunofluorescence confocal microscopy revealed that NPC1 colocalized with LAMP2 (Fig.
229 4E), and no difference of Pearson correlation coefficient was detected by high-content imaging
230 quantification (Fig. 4F). In contrast, a mislocalization of NPC2 from the lysosomes was observed
231 in the CoV-2-ORF3a cells (Fig. 4G), reproduced in a quantitative measurement of Pearson
232 correlation coefficient between NPC2 and LAMP1 (Fig. 4H). This mislocalization was largely
233 rescued by the W193A mutant (Fig. 4G,H). Further analysis of protein secretion revealed an
234 increased level of NPC2 and another lysosomal lumenal protein, cathepsin D, in the culture
235 media of CoV-2-ORF3a cells (Fig. 4I,J). These results motivated us to test whether lysosomal
236 transmembrane proteins, such as LAMPs, can localize to the lysosomes. Distinct from lysosomal
237 transmembrane proteins that are transported from TGN to lysosomes through biosynthesis
238 pathway, Ragulator complex is associated with lysosome membrane through lipidation of its
239 subunit LAMTOR1, which scaffolds other subunits. By measuring the colocalization between
240 LAMP2 and the Ragulator subunit LAMTOR4, we did not see a difference between the Flp-In

241 cells (Fig. S4H,I). Together, these results indicated that ORF3a induces a trafficking defect of
242 lysosome lumenal proteins, likely due to a dysregulation of protein transport between TGN and
243 endosomes.
244
245 **ORF3a disturbs the endosome-to-TGN transport**
246 The NPC2 trafficking defect observed in CoV-2-ORF3a cells resembled what was observed in
247 VPS39-deleted cells in our previous study, in which the sorting receptor for lysosomal lumenal
248 proteins, CI-MPR, is abnormally degraded in lysosomes[18]. In CoV-2-ORF3a cells, CI-MPR
249 protein level did not reduce (Fig. S4F), but it dispersed from its usual location near the
250 microtubule-organizing center (MTOC) to the cell periphery (Fig. 5A). In addition, a more
251 severe dispersion of the TGN protein TGN46 was observed in CoV-2-ORF3a cells (Fig. 5A). The
252 positioning changes of CI-MPR and TGN46 was confirmed by high-content imaging analysis
253 (Fig. 5B,C), in which cellular area between MTOC and cell boundary was divided into "center",
254 "middle", and "periphery" to reflect protein cellular distribution[52]. We also examined Golgi
255 matrix protein 130 (GM130) but did not see a dispersion (Fig. S5A), indicating that the
256 dispersion of CI-MPR and TGN46 in the Flp-in cells was not due to Golgi fragmentation[53,54]}.
257 The dispersed CI-MPR and TGN46 were partially colocalized with LAMP2 (Fig. 5A, arrows),
258 and quantitative results showed an increased Pearson correlation coefficient between CI-MPR
259 and LAMP2 (Fig. 5D). Consistently, CoV-2-ORF3a cells had an increased localization between
260 TGN46 and Rab7 (Fig. 5SB,C). These results indicate that CI-MPR and TGN46 were retained
261 within the Rab7- or LAMP2-positive endosomes and lysosomes in the CoV-2-ORF3a cells,
262 suggesting that TGN-to-endosome transport was increased, and/or retrieval from endosomes
263 and lysosomes was decreased, resulting in protein prolonged retention within the endosome-
264 lysosome system.
265
266 Retrieval of endosomal proteins relies on the retromer[16,55] and retriever[56] complexes. KO of
267 their shared subunit VPS29 resembled the defects observed in CoV-2 ORF3a cells, including
268 increased NPC2 secretion (Fig. 5E,F), lysosomal cholesterol accumulation (Fig. 5G), and
269 enhanced colocalization of CI-MPR and TGN46 with LAMP1 (Fig. 5H,I). These results indicate
270 that disruption of endosomal protein retrieval impairs lysosome cholesterol egress. We next
271 examined the Flp-In cells and found that the retromer subunit VPS35, which mediates
272 endosome-to-Golgi transport, exhibited increased colocalization with LAMP2 in CoV-2-ORF3a
273 cells (Fig. 5J, arrows). High-content imaging quantification showed an elevated Pearson's
274 correlation coefficient between VPS35 and LAMP2, which was rescued in W193A cells (Fig. 5K).
275 Together, these findings indicate that the ORF3a-VPS39 interaction disrupts endosome-to-TGN

276 transport by retaining retromer in LAMP2-positive endosomes/lysosomes, resulting in reduced
277 recycling of CI-MPR and targeting of NPC2 to lysosomes.
278
279 **ORF3a reduced BMPs**
280 BMPs, localized exclusively on late endosome and lysosome membranes, physically interacts
281 with NPC2 to facilitate cholesterol egress[33,34]. Using an antibody against BMPs[26], we observed
282 a significant reduction in BMP levels in SARS-CoV-2-infected Vero E6 cells, starting 12 hours
283 post-infection (Fig. 6A,B). To test if this alteration was related to ORF3a, we examined the Flp-In
284 cells and found that the BMP level was reduced by 20% in CoV-2-ORF3a cells, compared to the
285 control cells. This reduction was partially rescued in W193A cells, while the CoV-ORF3a cells
286 exhibited no change (Fig. 6C,D). Shotgun lipidomics of total lipids extracted from the Flp-In
287 cells confirmed these results: the two most abundant BMP species, 18:1-18:1 and 18:1-22:6, were
288 reduced by approximately 20% in CoV-2-ORF3a cells and restored in W193A cells (Fig. 6E).
289 These results indicate that CoV-2-ORF3a alone can decrease BMP levels, which is dependent on
290 the ORF3a-VPS39 interaction, aligned with the observed cholesterol sequestration. Furthermore,
291 exogenous BMP treatment for 2 hours in serum-free media decreased the lysosomal cholesterol
292 levels by 25% in CoV-2-ORF3a cells (Fig. 5F). Together, these results suggest that reduced BMP
293 is an additional mechanism underlying SARS-CoV-2-induced cholesterol sequestration.
294
295 **ORF3a interrupted lysosome-mitochondrion interaction**
296 To investigate the mechanism underlying BMP reduction, we examined key enzymes involved
297 in BMP biosynthesis and turnover, including CLN5[37], PLD3, PLD4[38], ABHD6[35], and
298 PLA2G15[39]. With the exception of PLA2G15, which did not display a punctate pattern upon
299 transfection, we did not observe a reduced colocalization with lysosomes (Fig. S6A-H) or
300 reduced expression levels (Fig. S6I) of these proteins, suggesting these enzymes are not
301 responsible for the BMP reduction in CoV-2-ORF3a cells.
302
303 We then isolated the lysosomes by Lyso-IP[57] followed by mass spectrometry of lysosomal
304 proteomes from the control, CoV-2-ORF3a and W193A Flp-In cells (Tab. 1). Comparison
305 revealed 277 proteins uniquely present in CoV-2-ORF3a samples (gained, Tab. 2), and 348
306 proteins increased at least 2-fold relative to W193A cells (increased, Tab. 3). In contrast, 160
307 proteins were undetected (lost, Tab. 2), and 87 proteins decreased by ≥50% in CoV-2-ORF3a
308 samples (decreased, Tab. 3). Gene ontology analysis using DAVID Bioinformatics indicated that
309 the gained and increased proteins largely originated from cytoplasm (32%) and nuclei (25%)
310 (Fig. 7A), while the lost and decreased proteins were predominantly mitochondrial (45%) and

311 ER-derived (21%) (Fig. 7B,C,D). Among the top 20% of lost proteins, 43.7% proteins were
312 mitochondrial, including outer membrane, inner membrane, and matrix proteins (Fig. 7C).
313 Similarly, in the reduced proteins, the majority was from mitochondria, regardless their
314 mitochondrial localization (Fig. 7D). These results suggest a reduced lysosome-mitochondrion
315 interaction in CoV-2-ORF3a cells.
316
317 Confocal imaging showed frequent lysosome–mitochondria interactions in control cells (Fig. 7E,
318 upper, arrows), while CoV-2 ORF3a cells exhibited fewer physical contacts, though organelles
319 remained proximal (Fig. 7E, lower). To quantify the physical interactions, we defined the
320 cytoplasm area in each cell and excluded the perinuclear clouds to reduce the false overlap due
321 to a usual crowdedness of organelles at that area (Fig. 7F). Indicated by Pearson correlation
322 coefficient, the interactions between mitochondria and lysosomes was significantly decreased in
323 the CoV-2-ORF3a cells and was rescued in the W193A cells (Fig. 7G). High-content imaging of
324 TOMM20 revealed slightly increased mitochondrial abundance and similar morphology in both
325 CoV-2-ORF3a and W193A cells (Fig. S7A,B,C), confirming that the reduced lysosome-
326 mitochondrion interaction was not due to fewer mitochondria or altered mitochondrial
327 morphology.
328
329 We hypothesized that impaired mitochondrion-lysosome interaction may limit mitochondrial
330 transportation of PGs, the precursors for BMP biosynthesis. Lipidomics revealed unchanged PG
331 levels among the three cell types, but mitochondrial cardiolipin, a PG derivative, increased in
332 CoV-2 ORF3a cells (Fig. 7H), suggesting that interrupted PG exportation from mitochondria
333 resulted in an increased local PG conversion and decreased BMP synthesis in lysosomes.
334
335 **ORF3a disturbed mitochondrion-lysosome membrane contact sites**
336 The direct physical interactions between mitochondria and lysosomes can be achieved through
337 autophagy, mitochondrion-derived vesicles (MDVs), and mitochondrion-lysosome membrane
338 contact sites (MCS). It was shown that autophagy flux is interrupted by ORF3a-VPS39
339 interaction, which inhibits HOPS-mediated fusion between autophagosomes and lysosomes[32].
340 We observed the same defect shown as increased LC3-II levels in CoV-2-ORF3a cells (Fig. S8A).
341 However, inhibiting autophagy fusion by STX17 KO (Fig. 8A), or interrupting earlier autophagy
342 steps by knockdown (KD) of ATG5, ATG7, or ULK1 (Fig. 8C) did not alter BMP levels (Fig.
343 8B,D). These results excluded autophagy as a PG transport pathway.
344

345 We next tested MDVs, identified by a combined staining of the MDV marker TOMM20 and a
346 mitochondrial but not MDV protein, pyruvate dehydrogenase (PDH) (Fig. 8E, arrows). We also
347 included a lysosome marker to visualize the fusion between MDV and lysosomes (Fig. 8E,
348 circles). CoV-2-ORF3a cells exhibited more MDVs and MDV-lysosome fusion events (Fig. 8F,G),
349 which did not align with the BMP reduction (Fig. 6C). Furthermore, KD of MDV biogenesis
350 genes, DRP1 or MIRO1/2[58] (Fig. 8H), did not decrease BMP levels (Fig. 8I), indicating that
351 MDVs do not mediate PG delivery to lysosomes.
352
353 Last, we applied electron microscopy to assess mitochondrion-lysosome MCS. We randomly
354 chose cells at low magnification and image areas containing abundant mitochondria at higher
355 magnification. Lysosome-to-mitochondrion ratios were similar across cell types (Fig. S8B), but
356 MCS events, identified by intact membrane within 10 to 30 nm distance (Fig. 8J), decreased in
357 CoV-2-ORF3a cells and were rescued in the W193A cells, though it was not statistically
358 significant (Fig. 8K). VPS39 is known to mediate the MCS formation in a HOPS-independent
359 manner in yeast[59]. Consistently, VPS39 KO decreased TOMM20-LAMP2 overlap and BMP
360 level, whereas VPS29, VPS41, or Rab7 KO did not (Fig. 8L,M). There findings suggest that
361 ORF3a inhibited VPS39-mediated lysosome-mitochondrion MCS formation and impaired PG
362 transportation, consequently reducing BMP synthesis.

363 **DISCUSSION**
364
365 Our study identifies SARS-CoV-2 ORF3a as a potent disruptor of lysosomal cholesterol
366 transport through dual interference with NPC2 trafficking and BMP biogenesis. By binding
367 VPS39, ORF3a blocks retromer-mediated retrieval of CI-MPR and reduces mitochondrion-to-
368 lysosome lipid transfer, thereby sequestering cholesterol within lysosomes. These findings
369 expand our understanding of cellular cholesterol regulation and the functions of HOPS and
370 VPS39, point to a regulatory pathway for BMP biosynthesis, and reveal a viral strategy that
371 links lysosomal lipid metabolism to SARS-CoV-2 pathogenesis.
372
373 Cholesterol is not only a structural component of cellular membranes but also a dynamic
374 signaling molecule whose intracellular distribution dictates multiple metabolic pathways. Our
375 results demonstrate that SARS-CoV-2 impedes lysosomal cholesterol egress (Fig. 1), adding to
376 the growing recognition that compartmentalized cholesterol pools, rather than bulk cholesterol,
377 drive cellular physiology[60,61]. ORF3a's ability to retain cholesterol within lysosomes (Figs.
378 2&4C,D) reveals a new viral strategy to manipulate host lipid homeostasis and may explain
379 systemic lipid alterations in COVID-19 patients[1–5]. More broadly, our findings place lysosomal
380 cholesterol transport at the crossroads of host–pathogen interactions and suggest that this
381 pathway may represent a therapeutic vulnerability.
382
383 BMPs play essential roles in lysosomal biology and have been implicated in a wide range of
384 human diseases[27,28], such as infectious disease[30,32,62,63], and neurodegenerative disorders[64,65].
385 Here, we demonstrate that SARS-CoV-2 and its ORF3a protein reduce BMP levels (Fig. 6A-E),
386 and that restoring BMP partially rescues cholesterol egress (Fig. 6F). This finding highlights
387 BMP as a limiting factor for lysosomal cholesterol export, in agreement with prior studies[33,33,34].
388 Notably, ORF3a alters PG metabolism by decreasing its lysosomal products (BMPs) and
389 increasing its mitochondrial products (cardiolipins) (Fig. 7H). This shift uncovers a previously
390 unrecognized regulatory mechanism in BMP homeostasis, the supply of mitochondrial
391 precursors. While BMP levels were thought to be controlled primarily by lysosomal synthetase
392 and hydrolases[35,37–39], our data suggest that cross-organelle lipid transfer provides an
393 additional layer of regulation. Importantly, by testing multiple possible routes, we found that
394 mitochondrion-lysosome membrane contact sites likely serve as the pathway for PG transport,
395 rather that autophagy or mitochondrial-derived vesicles (Fig. 8). These finding establish BMP
396 regulation as a point of crosstalk between mitochondrial phospholipid metabolism and

397 lysosomal cholesterol transport, with broad implications for both cellular physiology and viral
398 pathogenesis.
399
400 The canonical view of HOPS has centered on its role as a tethering complex that mediates late
401 endosome–lysosome and autophagosome–lysosome fusion[17]. By leveraging the VPS39–ORF3a
402 interaction and the W193A mutant, our study expands this paradigm by showing that VPS39
403 also regulates two distinct aspects of lysosomal activities, regulation of retromer-dependent
404 trafficking[66] (Fig. 5) and formation of mitochondrion–lysosome membrane contact sites
405 necessary for BMP synthesis (Fig. 8J-M). These findings position VPS39 as a multifunctional
406 coordinator at the lysosome, integrating protein trafficking and lipid exchange. The dual
407 disruption of these VPS39-dependent functions by ORF3a reframes HOPS/VPS39 not solely as
408 a fusion mediator, but as a broader regulatory hub essential for lysosomal homeostasis.
409
410 Our study establishes ORF3a as a viral effector that directly manipulates host lipid metabolism.
411 Unlike SARS-CoV ORF3a[67], its SARS-CoV-2 counterpart acquired the ability to bind
412 VPS39[43,44,68], suggesting an evolutionary adaptation to exploit lysosomal cholesterol regulation.
413 Since plasma membrane cholesterol promotes SARS-CoV-2 entry[11,12], restricting cholesterol
414 export from lysosomes could reduce cholesterol at the plasma membrane and thereby limit the
415 viral entry. Consistent with this model, pharmacological blockade of NPC1 with U18666A
416 sequesters cholesterol in lysosomes and decreases SARS-CoV-2 infection (Fig. S8C–E). In
417 addition, BMPs are required for viral fusion within endosomes/lysosomes[63], and reduced BMP
418 levels may impair this step of the viral life cycle. Importantly, ORF3a is an accessory protein
419 that is not incorporated into virions but translated only after infection from viral subgenomic
420 RNAs[69]. Thus, its interference with cholesterol export and BMP synthesis is unlikely to affect
421 the current infection but may restrict secondary infection events. Furthermore, ORF3a's
422 previously reported activities, including increasing lysosomal pH and damaging lysosomal
423 membranes, may promote lysosome exocytosis, a route for viral egress[42,70]. Taken together,
424 these findings suggest that SARS-CoV-2 use ORF3a to modulate multiple lysosomal functions,
425 integrating cholesterol trafficking, lipid metabolism, and membrane dynamics to optimize
426 different stages of its life cycle.
427
428 Our study has several limitations. First, although we demonstrate ORF3a-induced cholesterol
429 sequestration and identify VPS39-dependent mechanisms, the downstream consequences for
430 viral replication, immune responses, and cell survival remain to be fully elucidated *in vivo*.
431 Second, while we observed reduced mitochondrion–lysosome contacts and altered BMP levels,

432 the molecular intermediates mediating phosphatidylglycerol transfer remain undefined.
433 Finally, the interplay between cholesterol sequestration and systemic lipid dysregulation
434 observed in COVID-19 patients requires further integration with clinical data. Notably, SARS-
435 CoV-2 infects hepatocytes[71], and given the conserved role of HOPS in lysosomal trafficking,
436 similar lipid defects may occur in the liver, a central regulator of cholesterol and lipoprotein
437 metabolism. Future work will therefore examine hepatocytes to determine whether ORF3a-
438 mediated lysosomal disruptions contribute to the lipoprotein abnormalities observed in
439 COVID-19 and long COVID.
440
441 In summary, this work uncovers cholesterol transport and BMP biogenesis as dual regulatory
442 nodes governed by VPS39 and reveals how SARS-CoV-2 ORF3a exploits these pathways to
443 rewire lysosomal lipid metabolism. These findings advance fundamental understanding of
444 lysosomal protein trafficking and lysosome–mitochondrion crosstalk, broaden the functional
445 repertoire of HOPS/VPS39, and provide new perspectives on viral pathogenesis and
446 cholesterol-related diseases.

447 **MATERIALS AND METHODS**
448

449 **Cells and virus**

450 A549 and HeLa cells were cultured in Dulbecco's Modified Eagle's Medium (DMEM)
451 supplemented with 10% heat-inactivated fetal bovine serum (FBS), 25 mM HEPES, and
452 MycoZap Plus-CL (Lonza, Basel, Switzerland) at 37°C with 5% CO_2. Vero E6 cells (ATCC, CRL-
453 1586) were cultured in DMEM supplemented with 10% heat-inactivated FBS, 1% pen/strep,
454 2mM L-glut, 1% non-essential amino acids, 1% HEPES. Severe acute respiratory syndrome
455 coronavirus 2 (SARS-CoV-2, Isolate USA-WA1/2020) was acquired from BEI Resources (NR-
456 52281) and propagated in Vero E6 cells for 3 days. Infectious virus was isolated by harvesting
457 cellular supernatant and spinning at 1000 g for 10 minutes to remove cellular debris and stored
458 at -80°C. SARS-CoV-2 infectious particles were quantified in media by standard plaque assay[72]
459

460 **SARS-CoV-2 infections**

461 Coverslips or optic 96-well plates (Agilent, Santa Clara, CA) were coated with collagen solution
462 (0.03-0.04 mg/ml collagen in 0.02 N acetic acid) for > 30 min and then washed twice with PBS
463 before receiving cells. A549-hACE2 cells were seeded on coverslips at 0.1 X 10^6 cells per well or
464 in optical 96-well plates at 0.012 X 10^6 cells per well and infected with SARS-CoV-2 in DMEM
465 (4% FBS) at MOI: 4 and incubated at 37°C for 1 hr on the next day. Cells were then washed
466 twice with 1x PBS and normal culture media was added. At the indicated times post-infection,
467 cells were fixed with 4% PFA. Vero E6 cells were seeded in optical 96-well plate around 0.025 X
468 10^6 cells per well and infected with SARS-CoV-2 at MOI: 0.1 in 2% FBS media. The control group
469 of cells were incubated with the media only.
470

471 **Plasmid and siRNA transfection**

472 Cells were seeded a day before transfection and receive plasmids mixed with transfection
473 reagent Lipofectamine 2000 (Thermo Fisher Scientific) or TransIT-LT1 (Mirus Bio, Madison, WI),
474 following the manufactures' instructions. Cells were analyzed at 24- or 48-h post transfection.
475 On-TARGETplus SMARTpool siRNAs were applied (Horizon Discovery, Cambridge, UK) for
476 two-shot transfection at Day 1 and Day 3 after seeding. The transfection reagents Lipofectamine
477 2000 (Thermo Fisher Scientific) or TransIT-X2 (Mirus Bio) were used to deliver siRNA, and cells
478 were analyzed 6-7 days after seeding.
479

480 **CRISPR KO**

481 Genes were edited using the CRISPR/Cas9 system. Guide RNAs (gRNAs) were designed using
482 Benchling () Four to six 20-base pair (bp) gRNAs were selected and tested for the cleavage in

483 pilot experiments. gRNA was introduced into the px458 plasmid containing GFP sequence
484 (Addgene, Cambridge, MA). Cells were transfected with the plasmids, and GFP-positive cells
485 were collected by cell sorter 48 h after transfection. Transformants were kept in normal
486 medium for another 12 days to allow single colony formation. Genomic DNA was extracted
487 from individual colonies, and cleavage of the target sequence was tested by PCR followed by
488 Sanger sequencing and immunoblotting. Three to six single colonies were pooled for
489 experiment use.
490 Guide RNA target sequences used in this study:
491 Rab7 KO: TAGTTTGAAGGATGACCTCT and TTGCTGAAGGTTATCATCCT
492 VPS29 KO: GCAAACTGTTGCACCGGTGT and CATAACTCTCTTTGGTGCAA
493 Stx17 KO: TGGAGAAGACAGCTGTTACCAGGG and TTAAGATAGTAATCCCAACAGACC
494
495 **Generation of flip-in cells**
496 HeLa Flp-In host cells (Thermo Fisher Scientific, Waltham, MA) were transfected with the
497 plasmids encoding FLAG-tagged proteins or linker peptide and subjected to hygromycin
498 selection after 48 h post transfection in DMEM as described above but replacing regular FBS
499 with tetracycline-free FBS (Thermo Fisher Scientific) (tet-free media). Following 2-week
500 selection, transformants were kept in tet-free medium for another 12 days to allow single colony
501 formation. Protein expression was induced by addition of 1 μg/ml doxycycline for 16 hours.
502 The colonies had relatively low expression levels of FLAG were chosen and pooled for
503 experiments, determined by immunoblotting of FLAG.
504
505 **Immunofluorescence, Filipin staining, and confocal microscopy**
506 Fixed cells were washed 3 times with PBS, and primary antibodies were diluted in 1% BSA in
507 PBS supplemented with 0.2% saponin and applied to cells for 1 h at 37°C or overnight at 4°C.
508 Alexa-conjugated secondary antibodies (Thermo Fisher Scientific) were applied with the same
509 saponin-contained BSA-PBS solution for 30 min at 37°C. Coverslips were mounted with DAPI-
510 contained mounting reagents (Electron Microscopy Sciences, Hatfield, PA) and allowed to dry
511 at 37°C for at least 1 h. To stain free cholesterol, 25 μg/ml filipin complex (Millipore Sigma, St.
512 Louis, MO) in PBS was applied to fixed cells at 37°C for 30 min. When immunostaining was
513 performed with filipin, primary antibodies and Alexa-conjugated secondary antibodies along
514 with DRAQ7 (Novus Biologicals, Centennial, CO) were sequentially applied to filipin-stained
515 cells without detergent permeabilization. Then cells were mounted with mounting reagents
516 without DAPI (Electron Microscopy Sciences) at 37°C for at least 1 h. Images were acquired
517 using a Zeiss LSM800 confocal microscope equipped with the software ZEN (Zeiss,
518 Oberkochen, Germany).

519

520 **High-content imaging and image analysis**

521 Cells in optical 96-well plates were fixed and stained as described above and maintained in PBS
522 for immediate imaging. Imaging and analysis were performed using the CellInsight Microscope
523 platform (Thermo Fisher Scientific). DAPI- or DRAQ7-stained nuclei were scanned to determine
524 focus through the programmed autofocus function. Cytoplasmic signals from HCS CellMask
525 Near-IR Stain (Thermo Fisher Scientific) were applied to define individual cell boundaries. Cells
526 were excluded based on criteria including incomplete cell boundaries at image edges, abnormal
527 size or shape, and signs of cell death.

528

529 For cellular punctum analysis, the cell boundary-enclosed areas are defined as ROI_A. Filipin,
530 LAMP, or BMP puncta were detected as spots (2 pixels in size) using the software "spot
531 detection" function. Line-shaped filipin signals from the plasma membrane were excluded by
532 setting the validation criteria for shape. Puncta that overlapped with ROI_A were quantified by
533 their fluorescence intensity. To measure colocalized signals, the software function of
534 "colocalization" was applied, and the output feature "ROI_A(B) Correlation Coefficient" was
535 extracted for the quantification of Pearson Correlation Coefficient.

536

537 To analyze the infected cells, fixed cells were immunostained with an dsRNA antibody, and its
538 signals were used to set the threshold for detection of infected cells, using the function
539 "Reference" of the software.

540

541 **Sample Processing for electron microscopy**

542 Cells on glass coverslips were fixed in 0.1 M PIPES buffer containing 3% formaldehyde, 2%
543 glutaraldehyde, and 1.5 mM CaCl2, then washed in several buffer changes before secondary
544 fixation in 0.1 M PIPES containing: 1% osmium tetroxide for 15 min, 5 min PIPES rinse, 15 min
545 1% carbohydrazide in PIPES, 5 min PIPES rinse, and 15 min 1% osmium tetroxide (OCO).
546 Samples were then washed with buffer, followed by ultrapure water, before being dehydrated
547 through a graded series of ethanol to propylene oxide, infiltrated with Epon-Araldite resin,
548 embedded, and heat-cured. The glass was removed from the cured resin blocks so the cells
549 could be re-mounted for en face sectioning. Thin sections (60-80 nm) were mounted on Cu
550 grids, post-stained with uranyl acetate and Reynold's lead citrate, and examined in a Hitachi
551 HT7700 TEM operated at 80 kV. Images were captured with an AMT XR-81 CCD camera.

552

553 **Cholesterol measurement by GC-MS**

554 Cells were collected in PBS with a cell scraper after washing twice with PBS, and the total lipids
555 were extracted by adding lipid-extraction solvent (chloroform:methanol:acetic acid = 50:50:1) of
556 90% volume of PBS. The organic phase and aqueous phase were separated by 10 minute-
557 centrifugation at 21,000 g. Organic phase was collected and transferred into a new tube and
558 dried with vacuum. The extracted lipids were stored at -80°C for further analysis.
559 Cholesterol calibration standard solutions were prepared from the concentration of 50 μg/ml to
560 400 μg/ml along with 80 μg/ml 5a-cholestane as the internal standard. The linear calibration
561 curve was obtained with R2 =0.9884. The dried lipids were dissolved with hexane and mixed
562 with 4 μg 5a-cholestane. The GC-MS analysis was conducted on Agilent 6890/5973 with
563 selected ion monitoring (SIM) mode.
564
565 **Shotgun Lipidomics**
566 Lipid species were analyzed using a multidimensional mass spectrometry-based shotgun
567 lipidomics approach[73]. In brief, each cell sample homogenate containing 0.3 mg of protein
568 which was determined with a Pierce BCA assay was accurately transferred to a disposable glass
569 culture test tube. A premixture of lipid internal standards was added prior to conducting lipid
570 extraction for quantification of the targeted lipid classes. Lipid extraction was performed using
571 a modified Bligh and Dyer procedure (Wang and Han 2014), and each lipid extract was
572 reconstituted in chloroform:methanol (1:1, v:v) at a volume of 400 μL/mg protein.
573 Derivatization of lipid extracts for analysis of free fatty acid (FFA) and
574 bis(monoacylglycero)phosphate (BMP) was performed as described previously[74,75] before
575 lipidomics analysis. Lyso-phosphatidylglycerol (LPG) in the aqueous phase was enriched using
576 a HybridSPE cartridge. After washing with methanol, lysophospholipids were eluted with
577 methanol/ammonia hydroxide (9:1), dried and reconstituted in methanol for lipidomics
578 analysis [76]. For shotgun lipidomics, individual lipid samples prepared as aforementioned was
579 further diluted to a final concentration of ~500 fmol total lipids per μL. Mass spectrometric
580 analysis was performed on a triple quadrupole mass spectrometer (TSQ Altis, Thermo Fisher
581 Scientific, San Jose, CA) and a Q Exactive mass spectrometer (Thermo Scientific, San Jose, CA),
582 both of which were equipped with an automated nanospray device (TriVersa NanoMate,
583 Advion Bioscience Ltd., Ithaca, NY) as described[77]. Identification and quantification of lipid
584 species were performed using an automated software program[78,79]. Data processing (e.g., ion
585 peak selection, baseline correction, data transfer, peak intensity comparison, and quantitation)
586 was performed as described[79]. The results were normalized to the protein content (nmol
587 lipid/mg protein).
588

589 **Analysis of intracellular and extracellular proteins by Western blotting**
590 To detect secreted NPC2 and cathepsin D, cells were kept in a minimum volume of DMEM
591 without serum for 6 h after three-time washing with the same medium. The media were
592 collected and centrifuged at 1,000 g for 5 min to pellet any detached cells. The supernatants
593 were mixed with SDS loading buffer and subjected to SDS-PAGE and immunoblotting. After
594 collecting the media, cells were incubated in complete DMEM for 2 h. Cell lysates were
595 obtained by using 2X SDS sample buffer.
596
597 **Quantification and statistical analysis**
598 Image J was used for quantifying fluorescence signals of randomly-taken images from at least
599 three independent experiments. The signal intensity of vesicular filipin was measured using the
600 function of "Analyze particles", and co-localization was analyzed with the plug-in "PSC
601 Colocalization"[83]. High-content imaging results were obtained from more than 1,000 cells per
602 well and at least 3 wells per experiment. The number of trials is specified in the legends where
603 appropriate. The bar graphs show the pooled results displayed as mean ± SD. Colocalization
604 results include frequency distribution. Statistical significance was determined by comparing
605 two datasets using a *t* test with one-tailed distribution or more than two datasets using one-way
606 ANOVA, using the software Prism 9 (GraphPad). Probability values and number of trials are
607 given in the figure captions and the legends where appropriate. The statistical significance is
608 generally denoted as follows: *, $p < 0.05$, **, $p < 0.01$, ***, $p < 0.001$, ****, $p < 0.0001$, and n.s., not
609 significant.
610
611 **AUTHOR CONTRIBUTIONS**
612
613 J.P. conceived the project. B.G. and J.P. performed most of the experiments. V.M.V.
614 characterized VPS29-KO cells and performed secretion assays. O.K. quantified NPC2-LAMP1
615 colocalization. R.L. measured total cholesterol levels by GC-MS. J.J. made SARS-CoV-2 ORF3a
616 cell line. M.I. made VPS29-KO cells. H.W. and X.H. performed lipidomics analysis. A.K.
617 performed SARS-CoV-2 infection in A549 cells. C.Y. and S.B. performed the infection in Vero E6
618 cells. M.R.L. analyzed the structures of SARS-CoV and SARS-CoV-2 ORF3a. B.G. and J.P.
619 analyzed the data. J.P. wrote the manuscript. All the authors edited the manuscript.
620

621 **ACKNOWLEDGMENTS**

622 We thank A. Kajon for gift of A549-hACE2 cells, P. Lobel for mch-NPC2 construct and NPC2
623 antibody, J. Bonifacino for VPS29-KO HeLa cells, and J. Anderson for experimental assistance.
624 EM data were generated in the HSC-Electron Microscopy Facility, supported by University of
625 New Mexico Health Sciences Center (HSC). This research made use of the CellInsight
626 Microscope Platform and confocal microscope from Autophagy, Inflammation, and Metabolism
627 Center of Biomedical Research Excellence, funded by NIGMS, NIH (P20GM121176). Lipidomics
628 analysis was performed at Barshop Institute Functional Lipidomics Core funded by NIA, NIH
629 (P30AG013319). The funding support was from NIGMS, NIH (T32GM144834 and
630 R35GM147419).

631

632 **SUPPLEMENTAL INFORMATION**

633 Supplemental Information includes 8 figures and 3 tables.

634 **REFERENCES**

635 1. Li, Y., Zhang, Y., Lu, R., Dai, M., Shen, M., Zhang, J., Cui, Y., Liu, B., Lin, F., Chen, L., Han,
636 D., Fan, Y., Zeng, Y., Li, W., Li, S., Chen, X., Li, H. & Pan, P., Lipid metabolism changes in
637 patients with severe COVID-19. Clin Chim Acta 2021 517 33639119
638 2. Rezaei, A., Neshat, S. & Heshmat-Ghahdarijani, K., Alterations of Lipid Profile in COVID-
639 19: A Narrative Review. Curr Probl Cardiol 2022 47(3) 34272088
640 3. Zickler, M., Stanelle-Bertram, S., Ehret, S., Heinrich, F., Lange, P., Schaumburg, B.,
641 Kouassi, N. M., Beck, S., Jaeckstein, M. Y., Mann, O., Krasemann, S., Schroeder, M.,
642 Jarczak, D., Nierhaus, A., Kluge, S., Peschka, M., Schlüter, H., Renné, T., Pueschel, K.,
643 Kloetgen, A., Scheja, L., Ondruschka, B., Heeren, J. & Gabriel, G., Replication of SARS-
644 CoV-2 in adipose tissue determines organ and systemic lipid metabolism in hamsters and
645 humans. Cell Metab 2022 34(1) 34895500
646 4. Xu, E., Xie, Y. & Al-Aly, Z., Risks and burdens of incident dyslipidaemia in long COVID: a
647 cohort study. Lancet Diabetes Endocrinol 2023 11(2) 36623520
648 5. López-Hernández, Y., Oropeza-Valdez, J. J., García Lopez, D. A., Borrego, J. C., Murgu,
649 M., Valdez, J., López, J. A. & Monárrez-Espino, J., Untargeted analysis in post-COVID-19
650 patients reveals dysregulated lipid pathways two years after recovery. Front Mol Biosci
651 2023 10 36936993
652 6. Luo, J., Yang, H. & Song, B. L., Mechanisms and regulation of cholesterol homeostasis. Nat
653 Rev Mol Cell Biol 2020 21(4) 31848472
654 7. Luo, J., Jiang, L. Y., Yang, H. & Song, B. L., Intracellular Cholesterol Transport by Sterol
655 Transfer Proteins at Membrane Contact Sites. Trends Biochem Sci 2019 44(3) 30415968
656 8. Meng, Y., Heybrock, S., Neculai, D. & Saftig, P., Cholesterol Handling in Lysosomes and
657 Beyond. Trends Cell Biol 2020 30(6) 32413315
658 9. Matsuo, H., Chevallier, J., Mayran, N., Le Blanc, I., Ferguson, C., Fauré, J., Blanc, N. S.,
659 Matile, S., Dubochet, J., Sadoul, R., Parton, R. G., Vilbois, F. & Gruenberg, J., Role of LBPA
660 and Alix in multivesicular liposome formation and endosome organization. Science 2004
661 303(5657) 14739459
662 10. Spector, A. A. & Yorek, M. A., Membrane lipid composition and cellular function. J Lipid
663 Res 1985 26(9) 3906008
664 11. Sanders, D. W., Jumper, C. C., Ackerman, P. J., Bracha, D., Donlic, A., Kim, H., Kenney, D.,
665 Castello-Serrano, I., Suzuki, S., Tamura, T., Tavares, A. H., Saeed, M., Holehouse, A. S.,
666 Ploss, A., Levental, I., Douam, F., Padera, R. F., Levy, B. D. & Brangwynne, C. P., SARS-
667 CoV-2 requires cholesterol for viral entry and pathological syncytia formation. Elife 2021
668 10 33890572
669 12. Wang, H., Yuan, Z., Pavel, M. A., Jablonski, S. M., Jablonski, J., Hobson, R., Valente, S.,
670 Reddy, C. B. & Hansen, S. B., The role of high cholesterol in SARS-CoV-2 infectivity. J Biol
671 Chem 2023 299(6) 37119851
672 13. Eskelinen, E. L., Schmidt, C. K., Neu, S., Willenborg, M., Fuertes, G., Salvador, N., Tanaka,
673 Y., Lüllmann-Rauch, R., Hartmann, D., Heeren, J., von Figura, K., Knecht, E. & Saftig, P.,
674 Disturbed cholesterol traffic but normal proteolytic function in LAMP-1/LAMP-2 double-
675 deficient fibroblasts. Mol Biol Cell 2004 15(7) 15121881
676 14. Popovic, K., Holyoake, J., Pomès, R. & Privé, G. G., Structure of saposin A lipoprotein
677 discs. Proc Natl Acad Sci U S A 2012 109(8) 22308394
678 15. Braulke, T. & Bonifacino, J. S., Sorting of lysosomal proteins. Biochim Biophys Acta 2009
679 1793(4) 19046998
680 16. Seaman, M. N., McCaffery, J. M. & Emr, S. D., A membrane coat complex essential for
681 endosome-to-Golgi retrograde transport in yeast. J Cell Biol 1998 142(3) 9700157
682 17. Solinger, J. A. & Spang, A., Tethering complexes in the endocytic pathway: CORVET and
683 HOPS. FEBS J 2013 280(12) 23351085
684 18. Anderson, J., Walker, G. & Pu, J., BORC-ARL8-HOPS ensemble is required for lysosomal
685 cholesterol egress through NPC2. Mol Biol Cell 2022 33(9) 35653304

686 19. Schleinitz, A., Pöttgen, L. A., Keren-Kaplan, T., Pu, J., Saftig, P., Bonifacino, J. S., Haas, A.
687 & Jeschke, A., Consecutive functions of small GTPases guide HOPS-mediated tethering of
688 late endosomes and lysosomes. Cell Rep 2023 42(1) 36640308
689 20. Bonifacino, J. S. & Hierro, A., Transport according to GARP: receiving retrograde cargo at
690 the trans-Golgi network. Trends Cell Biol 2011 21(3) 21183348
691 21. Willenborg, M., Schmidt, C. K., Braun, P., Landgrebe, J., von Figura, K., Saftig, P. &
692 Eskelinen, E. L., Mannose 6-phosphate receptors, Niemann-Pick C2 protein, and
693 lysosomal cholesterol accumulation. J Lipid Res 2005 46(12) 16177447
694 22. Wei, J., Zhang, Y. Y., Luo, J., Wang, J. Q., Zhou, Y. X., Miao, H. H., Shi, X. J., Qu, Y. X., Xu,
695 J., Li, B. L. & Song, B. L., The GARP Complex Is Involved in Intracellular Cholesterol
696 Transport via Targeting NPC2 to Lysosomes. Cell Rep 2017 19(13) 28658628
697 23. Carstea, E. D., Morris, J. A., Coleman, K. G., Loftus, S. K., Zhang, D., Cummings, C., Gu, J.,
698 Rosenfeld, M. A., Pavan, W. J., Krizman, D. B., Nagle, J., Polymeropoulos, M. H., Sturley,
699 S. L., Ioannou, Y. A., Higgins, M. E., Comly, M., Cooney, A., Brown, A., Kaneski, C. R.,
700 Blanchette-Mackie, E. J., Dwyer, N. K., Neufeld, E. B., Chang, T. Y., Liscum, L., Strauss, J.
701 F., Ohno, K., Zeigler, M., Carmi, R., Sokol, J., Markie, D., O'Neill, R. R., van Diggelen, O.
702 P., Elleder, M., Patterson, M. C., Brady, R. O., Vanier, M. T., Pentchev, P. G. & Tagle, D. A.,
703 Niemann-Pick C1 disease gene: homology to mediators of cholesterol homeostasis. Science
704 1997 277(5323) 9211849
705 24. Naureckiene, S., Sleat, D. E., Lackland, H., Fensom, A., Vanier, M. T., Wattiaux, R., Jadot,
706 M. & Lobel, P., Identification of HE1 as the second gene of Niemann-Pick C disease.
707 Science 2000 290(5500) 11125141
708 25. Carette, J. E., Raaben, M., Wong, A. C., Herbert, A. S., Obernosterer, G., Mulherkar, N.,
709 Kuehne, A. I., Kranzusch, P. J., Griffin, A. M., Ruthel, G., Dal Cin, P., Dye, J. M., Whelan, S.
710 P., Chandran, K. & Brummelkamp, T. R., Ebola virus entry requires the cholesterol
711 transporter Niemann-Pick C1. Nature 2011 477(7364) 21866103
712 26. Kobayashi, T., Stang, E., Fang, K. S., de Moerloose, P., Parton, R. G. & Gruenberg, J., A
713 lipid associated with the antiphospholipid syndrome regulates endosome structure and
714 function. Nature 1998 392(6672) 9515966
715 27. Showalter, M. R., Berg, A. L., Nagourney, A., Heil, H., Carraway, K. L. & Fiehn, O., The
716 Emerging and Diverse Roles of Bis(monoacylglycero) Phosphate Lipids in Cellular
717 Physiology and Disease. Int J Mol Sci 2020 21 33137979
718 28. Medoh, U. N. & Abu-Remaileh, M., The Bis(monoacylglycero)-phosphate Hypothesis:
719 From Lysosomal Function to Therapeutic Avenues. Annu Rev Biochem 2024 93(1)
720 38603559
721 29. Le Blanc, I., Luyet, P. P., Pons, V., Ferguson, C., Emans, N., Petiot, A., Mayran, N.,
722 Demaurex, N., Fauré, J., Sadoul, R., Parton, R. G. & Gruenberg, J., Endosome-to-cytosol
723 transport of viral nucleocapsids. Nat Cell Biol 2005 7 15951806
724 30. Roth, S. L. & Whittaker, G. R., Promotion of vesicular stomatitis virus fusion by the
725 endosome-specific phospholipid bis(monoacylglycero)phosphate (BMP). FEBS Lett 2011
726 585(6) 21333650
727 31. Bissig, C., Lenoir, M., Velluz, M. C., Kufareva, I., Abagyan, R., Overduin, M. & Gruenberg,
728 J., Viral infection controlled by a calcium-dependent lipid-binding module in ALIX. Dev
729 Cell 2013 25(4) 23664863
730 32. Markosyan, R. M., Marin, M., Zhang, Y., Cohen, F. S. & Melikyan, G. B., The late
731 endosome-resident lipid bis(monoacylglycero)phosphate is a cofactor for Lassa virus
732 fusion. PLoS Pathog 2021 17(9) 34492091
733 33. Chevallier, J., Chamoun, Z., Jiang, G., Prestwich, G., Sakai, N., Matile, S., Parton, R. G. &
734 Gruenberg, J., Lysobisphosphatidic acid controls endosomal cholesterol levels. J Biol
735 Chem 2008 283(41) 18644787
736 34. McCauliff, L. A., Langan, A., Li, R., Ilnytska, O., Bose, D., Waghalter, M., Lai, K., Kahn, P.
737 C. & Storch, J., Intracellular cholesterol trafficking is dependent upon NPC2 interaction
738 with lysobisphosphatidic acid. Elife 2019 8 31580258

739 35. Pribasnig, M. A., Mrak, I., Grabner, G. F., Taschler, U., Knittelfelder, O., Scherz, B.,
740 Eichmann, T. O., Heier, C., Grumet, L., Kowaliuk, J., Romauch, M., Holler, S., Anderl, F.,
741 Wolinski, H., Lass, A., Breinbauer, R., Marsche, G., Brown, J. M. & Zimmermann, R., α/β
742 Hydrolase Domain-containing 6 (ABHD6) Degrades the Late Endosomal/Lysosomal
743 Lipid Bis(monoacylglycero)phosphate. J Biol Chem 2015 290(50) 26491015
744 36. Grabner, G. F., Fawzy, N., Pribasnig, M. A., Trieb, M., Taschler, U., Holzer, M., Schweiger,
745 M., Wolinski, H., Kolb, D., Horvath, A., Breinbauer, R., Rülicke, T., Rabl, R., Lass, A.,
746 Stadlbauer, V., Hutter-Paier, B., Stauber, R. E., Fickert, P., Zechner, R., Marsche, G.,
747 Eichmann, T. O. & Zimmermann, R., Metabolic disease and ABHD6 alter the circulating
748 bis(monoacylglycerol)phosphate profile in mice and humans. J Lipid Res 2019 60(5)
749 30894461
750 37. Medoh, U. N., Hims, A., Chen, J. Y., Ghoochani, A., Nyame, K., Dong, W. & Abu-
751 Remaileh, M., The Batten disease gene product CLN5 is the lysosomal
752 bis(monoacylglycero)phosphate synthase. Science 2023 381(6663) 37708259
753 38. Singh, S., Dransfeld, U. E., Ambaw, Y. A., Lopez-Scarim, J., Farese, R. V. & Walther, T. C.,
754 PLD3 and PLD4 synthesize S,S-BMP, a key phospholipid enabling lipid degradation in
755 lysosomes. Cell 2024 187(24) 39423811
756 39. Nyame, K., Xiong, J., Alsohybe, H. N., de Jong, A. P. H., Peña, I. V., de Miguel, R.,
757 Brummelkamp, T. R., Hartmann, G., Nijman, S. M. B., Raaben, M., Simcox, J. A., Blomen,
758 V. A. & Abu-Remaileh, M., PLA2G15 is a BMP hydrolase and its targeting ameliorates
759 lysosomal disease. Nature 2025 642(8067) 40335701
760 40. Cansell, M., Gouygou, J. P., Jozefonvicz, J. & Letourneur, D., Lipid composition of
761 cultured endothelial cells in relation to their growth. Lipids 1997 32(1) 9075191
762 41. Bar-On, Y. M., Flamholz, A., Phillips, R. & Milo, R., SARS-CoV-2 (COVID-19) by the
763 numbers. Elife 2020 9 32228860
764 42. Ghosh, S., Dellibovi-Ragheb, T. A., Kerviel, A., Pak, E., Qiu, Q., Fisher, M., Takvorian, P.
765 M., Bleck, C., Hsu, V. W., Fehr, A. R., Perlman, S., Achar, S. R., Straus, M. R., Whittaker, G.
766 R., de Haan, C. A. M., Kehrl, J., Altan-Bonnet, G. & Altan-Bonnet, N., β-Coronaviruses Use
767 Lysosomes for Egress Instead of the Biosynthetic Secretory Pathway. Cell 2020 183(6)
768 33157038
769 43. Miao, G., Zhao, H., Li, Y., Ji, M., Chen, Y., Shi, Y., Bi, Y., Wang, P. & Zhang, H., ORF3a of
770 the COVID-19 virus SARS-CoV-2 blocks HOPS complex-mediated assembly of the SNARE
771 complex required for autolysosome formation. Dev Cell 2021 56(4) 33422265
772 44. Zhang, Y., Sun, H., Pei, R., Mao, B., Zhao, Z., Li, H., Lin, Y. & Lu, K., The SARS-CoV-2
773 protein ORF3a inhibits fusion of autophagosomes with lysosomes. Cell Discov 2021 7(1)
774 33947832
775 45. Miller, A. N., Houlihan, P. R., Matamala, E., Cabezas-Bratesco, D., Lee, G. Y., Cristofori-
776 Armstrong, B., Dilan, T. L., Sanchez-Martinez, S., Matthies, D., Yan, R., Yu, Z., Ren, D.,
777 Brauchi, S. E. & Clapham, D. E., The SARS-CoV-2 accessory protein Orf3a is not an ion
778 channel, but does interact with trafficking proteins. Elife 2023 12 36695574
779 46. Kern, D. M., Sorum, B., Mali, S. S., Hoel, C. M., Sridharan, S., Remis, J. P., Toso, D. B.,
780 Kotecha, A., Bautista, D. M. & Brohawn, S. G., Cryo-EM structure of SARS-CoV-2 ORF3a
781 in lipid nanodiscs. Nat Struct Mol Biol 2021 28(7) 34158638
782 47. Dolan, K. A., Dutta, M., Kern, D. M., Kotecha, A., Voth, G. A. & Brohawn, S. G., Structure
783 of SARS-CoV-2 M protein in lipid nanodiscs. Elife 2022 11 36264056
784 48. Andrews, B. J., Proteau, G. A., Beatty, L. G. & Sadowski, P. D., The FLP recombinase of the
785 2 micron circle DNA of yeast: interaction with its target sequences. Cell 1985 40(4) 3879971
786 49. Argos, P., Landy, A., Abremski, K., Egan, J. B., Haggard-Ljungquist, E., Hoess, R. H.,
787 Kahn, M. L., Kalionis, B., Narayana, S. V. & Pierson, L. S., The integrase family of site-
788 specific recombinases: regional similarities and global diversity. EMBO J 1986 5(2) 3011407
789 50. Jia, J., Wang, F., Bhujabal, Z., Peters, R., Mudd, M., Duque, T., Allers, L., Javed, R., Salemi,
790 M., Behrends, C., Phinney, B., Johansen, T. & Deretic, V., Stress granules and mTOR are

791 regulated by membrane atg8ylation during lysosomal damage. J Cell Biol 2022 221(11)
792 36179369
793 51. Jia, J., Claude-Taupin, A., Gu, Y., Choi, S. W., Peters, R., Bissa, B., Mudd, M. H., Allers, L.,
794 Pallikkuth, S., Lidke, K. A., Salemi, M., Phinney, B., Mari, M., Reggiori, F. & Deretic, V.,
795 Galectin-3 Coordinates a Cellular System for Lysosomal Repair and Removal. Dev Cell
796 2020 52(1) 31813797
797 52. Kolaczkowski, O. M., Goodson, B. A., Vazquez, V. M., Jia, J., Bhat, A. Q., Kim, T. H. & Pu,
798 J., Synergistic Role of Amino Acids in Enhancing mTOR Activation Through Lysosome
799 Positioning. bioRxiv 2024 39416115
800 53. Tang, D., Mar, K., Warren, G. & Wang, Y., Molecular mechanism of mitotic Golgi
801 disassembly and reassembly revealed by a defined reconstitution assay. J Biol Chem 2008
802 283(10) 18156178
803 54. Wei, J. H. & Seemann, J., Golgi ribbon disassembly during mitosis, differentiation and
804 disease progression. Curr Opin Cell Biol 2017 47 28390244
805 55. Seaman, M. N., Marcusson, E. G., Cereghino, J. L. & Emr, S. D., Endosome to Golgi
806 retrieval of the vacuolar protein sorting receptor, Vps10p, requires the function of the
807 VPS29, VPS30, and VPS35 gene products. J Cell Biol 1997 137(1) 9105038
808 56. McNally, K. E., Faulkner, R., Steinberg, F., Gallon, M., Ghai, R., Pim, D., Langton, P.,
809 Pearson, N., Danson, C. M., Nägele, H., Morris, L. L., Singla, A., Overlee, B. L., Heesom, K.
810 J., Sessions, R., Banks, L., Collins, B. M., Berger, I., Billadeau, D. D., Burstein, E. & Cullen,
811 P. J., Retriever is a multiprotein complex for retromer-independent endosomal cargo
812 recycling. Nat Cell Biol 2017 19(10) 28892079
813 57. Abu-Remaileh, M., Wyant, G. A., Kim, C., Laqtom, N. N., Abbasi, M., Chan, S. H.,
814 Freinkman, E. & Sabatini, D. M., Lysosomal metabolomics reveals V-ATPase- and mTOR-
815 dependent regulation of amino acid efflux from lysosomes. Science 2017 358(6364)
816 29074583
817 58. König, T., Nolte, H., Aaltonen, M. J., Tatsuta, T., Krols, M., Stroh, T., Langer, T. & McBride,
818 H. M., MIROs and DRP1 drive mitochondrial-derived vesicle biogenesis and promote
819 quality control. Nat Cell Biol 2021 23(12) 34873283
820 59. González Montoro, A., Auffarth, K., Hönscher, C., Bohnert, M., Becker, T., Warscheid, B.,
821 Reggiori, F., van der Laan, M., Fröhlich, F. & Ungermann, C., Vps39 Interacts with Tom40
822 to Establish One of Two Functionally Distinct Vacuole-Mitochondria Contact Sites. Dev
823 Cell 2018 45(5) 29870720
824 60. Ikonen, E. & Zhou, X., Cholesterol transport between cellular membranes: A balancing act
825 between interconnected lipid fluxes. Dev Cell 2021 56(10) 34004151
826 61. Johnson, K. A. & Radhakrishnan, A., Accessibility of cholesterol at cell surfaces. J Lipid
827 Res 2020 61(10) 32327483
828 62. Zaitseva, E., Yang, S. T., Melikov, K., Pourmal, S. & Chernomordik, L. V., Dengue virus
829 ensures its fusion in late endosomes using compartment-specific lipids. PLoS Pathog 2010
830 6(10) 20949067
831 63. Birtles, D., Abbas, W. & Lee, J., Bis(Monoacylglycero)Phosphate Promotes Membrane
832 Fusion Facilitated by the SARS-CoV-2 Fusion Domain. J Phys Chem B 2024 128(11)
833 38466655
834 64. Maloney, M. T., Wang, X., Ghosh, R., Andrews, S. V., Maciuca, R., Masoud, S. T., Agam,
835 M., Caprioli, R. M., Astarita, G., Bondar, V. V., Chen, J., Chiu, C. L., Davis, S. S., Ho, A. C.,
836 Nguyen, H. N., Propson, N. E., Reyzer, M. L., Davis, O. B., Deen, M. C., Zhu, S., Di Paolo,
837 G., Vocadlo, D. J., Estrada, A. A., de Vicente, J., Lewcock, J. W., Arguello, A., Suh, J. H.,
838 Huntwork-Rodriguez, S. & Henry, A. G., LRRK2 kinase activity regulates Parkinson's
839 disease-relevant lipids at the lysosome. Mol Neurodegener 2025 20(1) 40770658
840 65. Qureshi, Y. H., Patel, V. M., Berman, D. E., Kothiya, M. J., Neufeld, J. L., Vardarajan, B.,
841 Tang, M., Reyes-Dumeyer, D., Lantigua, R., Medrano, M., Jiménez-Velázquez, I. J., Small,
842 S. A. & Reitz, C., An Alzheimer's Disease-Linked Loss-of-Function CLN5 Variant Impairs

843 Cathepsin D Maturation, Consistent with a Retromer Trafficking Defect. Mol Cell Biol
844 2018 38(20) 30037983
845 66. Walia, K., Sharma, A., Paul, S., Chouhan, P., Kumar, G., Ringe, R., Sharma, M. & Tuli, A.,
846 SARS-CoV-2 virulence factor ORF3a blocks lysosome function by modulating TBC1D5-
847 dependent Rab7 GTPase cycle. Nat Commun 2024 15(1) 38448435
848 67. Shen, S., Lin, P. S., Chao, Y. C., Zhang, A., Yang, X., Lim, S. G., Hong, W. & Tan, Y. J., The
849 severe acute respiratory syndrome coronavirus 3a is a novel structural protein. Biochem
850 Biophys Res Commun 2005 330(1) 15781262
851 68. Gordon, D. E., Jang, G. M., Bouhaddou, M., Xu, J., Obernier, K., White, K. M., O'Meara, M.
852 J., Rezelj, V. V., Guo, J. Z., Swaney, D. L., Tummino, T. A., Hüttenhain, R., Kaake, R. M.,
853 Richards, A. L., Tutuncuoglu, B., Foussard, H., Batra, J., Haas, K., Modak, M., Kim, M.,
854 Haas, P., Polacco, B. J., Braberg, H., Fabius, J. M., Eckhardt, M., Soucheray, M., Bennett, M.
855 J., Cakir, M., McGregor, M. J., Li, Q., Meyer, B., Roesch, F., Vallet, T., Mac Kain, A., Miorin,
856 L., Moreno, E., Naing, Z. Z. C., Zhou, Y., Peng, S., Shi, Y., Zhang, Z., Shen, W., Kirby, I. T.,
857 Melnyk, J. E., Chorba, J. S., Lou, K., Dai, S. A., Barrio-Hernandez, I., Memon, D.,
858 Hernandez-Armenta, C., Lyu, J., Mathy, C. J. P., Perica, T., Pilla, K. B., Ganesan, S. J.,
859 Saltzberg, D. J., Rakesh, R., Liu, X., Rosenthal, S. B., Calviello, L., Venkataramanan, S.,
860 Liboy-Lugo, J., Lin, Y., Huang, X. P., Liu, Y., Wankowicz, S. A., Bohn, M., Safari, M., Ugur,
861 F. S., Koh, C., Savar, N. S., Tran, Q. D., Shengjuler, D., Fletcher, S. J., O'Neal, M. C., Cai, Y.,
862 Chang, J. C. J., Broadhurst, D. J., Klippsten, S., Sharp, P. P., Wenzell, N. A., Kuzuoglu-
863 Ozturk, D., Wang, H. Y., Trenker, R., Young, J. M., Cavero, D. A., Hiatt, J., Roth, T. L.,
864 Rathore, U., Subramanian, A., Noack, J., Hubert, M., Stroud, R. M., Frankel, A. D.,
865 Rosenberg, O. S., Verba, K. A., Agard, D. A., Ott, M., Emerman, M., Jura, N., von Zastrow,
866 M., Verdin, E., Ashworth, A., Schwartz, O., d'Enfert, C., Mukherjee, S., Jacobson, M.,
867 Malik, H. S., Fujimori, D. G., Ideker, T., Craik, C. S., Floor, S. N., Fraser, J. S., Gross, J. D.,
868 Sali, A., Roth, B. L., Ruggero, D., Taunton, J., Kortemme, T., Beltrao, P., Vignuzzi, M.,
869 García-Sastre, A., Shokat, K. M., Shoichet, B. K. & Krogan, N. J., A SARS-CoV-2 protein
870 interaction map reveals targets for drug repurposing. Nature 2020 583(7816) 32353859
871 69. Murigneux, E., Softic, L., Aubé, C., Grandi, C., Judith, D., Bruce, J., Le Gall, M.,
872 Guillonneau, F., Schmitt, A., Parissi, V., Berlioz-Torrent, C., Meertens, L., Hansen, M. M.
873 K. & Gallois-Montbrun, S., Proteomic analysis of SARS-CoV-2 particles unveils a key role
874 of G3BP proteins in viral assembly. Nat Commun 2024 15(1) 38245532
875 70. Chen, D., Zheng, Q., Sun, L., Ji, M., Li, Y., Deng, H. & Zhang, H., ORF3a of SARS-CoV-2
876 promotes lysosomal exocytosis-mediated viral egress. Dev Cell 2021 56(23) 34706264
877 71. Wanner, N., Andrieux, G., Badia-I-Mompel, P., Edler, C., Pfefferle, S., Lindenmeyer, M. T.,
878 Schmidt-Lauber, C., Czogalla, J., Wong, M. N., Okabayashi, Y., Braun, F., Lütgehetmann,
879 M., Meister, E., Lu, S., Noriega, M. L. M., Günther, T., Grundhoff, A., Fischer, N.,
880 Bräuninger, H., Lindner, D., Westermann, D., Haas, F., Roedl, K., Kluge, S., Addo, M. M.,
881 Huber, S., Lohse, A. W., Reiser, J., Ondruschka, B., Sperhake, J. P., Saez-Rodriguez, J.,
882 Boerries, M., Hayek, S. S., Aepfelbacher, M., Scaturro, P., Puelles, V. G. & Huber, T. B.,
883 Molecular consequences of SARS-CoV-2 liver tropism. Nat Metab 2022 4(3) 35347318
884 72. Mendoza, E. J., Manguiat, K., Wood, H. & Drebot, M., Two Detailed Plaque Assay
885 Protocols for the Quantification of Infectious SARS-CoV-2. Curr Protoc Microbiol 2020
886 57(1) 32475066
887 73. Han, X. *Lipidomics: Comprehensive mass spectrometry of lipids* (John Wiley & Sons, 2016).
888 74. Cheng, H., Jiang, X. & Han, X., Alterations in lipid homeostasis of mouse dorsal root
889 ganglia induced by apolipoprotein E deficiency: a shotgun lipidomics study. J Neurochem
890 2007 101(1) 17241120
891 75. Han, X., Yang, K., Cheng, H., Fikes, K. N. & Gross, R. W., Shotgun lipidomics of
892 phosphoethanolamine-containing lipids in biological samples after one-step in situ
893 derivatization. J Lipid Res 2005 46(7) 15834120
894 76. Wang, M. & Han, X., Multidimensional mass spectrometry-based shotgun lipidomics.
895 Methods Mol Biol 2014 1198 25270931

896 77. Han, X., Yang, K. & Gross, R. W., Microfluidics-based electrospray ionization enhances the
897 intrasource separation of lipid classes and extends identification of individual molecular
898 species through multi-dimensional mass spectrometry: development of an automated
899 high-throughput platform for shotgun lipidomics. Rapid Commun Mass Spectrom 2008
900 22(13) 18523984
901 78. Wang, M., Wang, C., Han, R. H. & Han, X., Novel advances in shotgun lipidomics for
902 biology and medicine. Prog Lipid Res 2016 61 26703190
903 79. Yang, K., Cheng, H., Gross, R. W. & Han, X., Automated lipid identification and
904 quantification by multidimensional mass spectrometry-based shotgun lipidomics. Anal
905 Chem 2009 81(11) 19408941
906

907 **FIGURES**

Figure 1

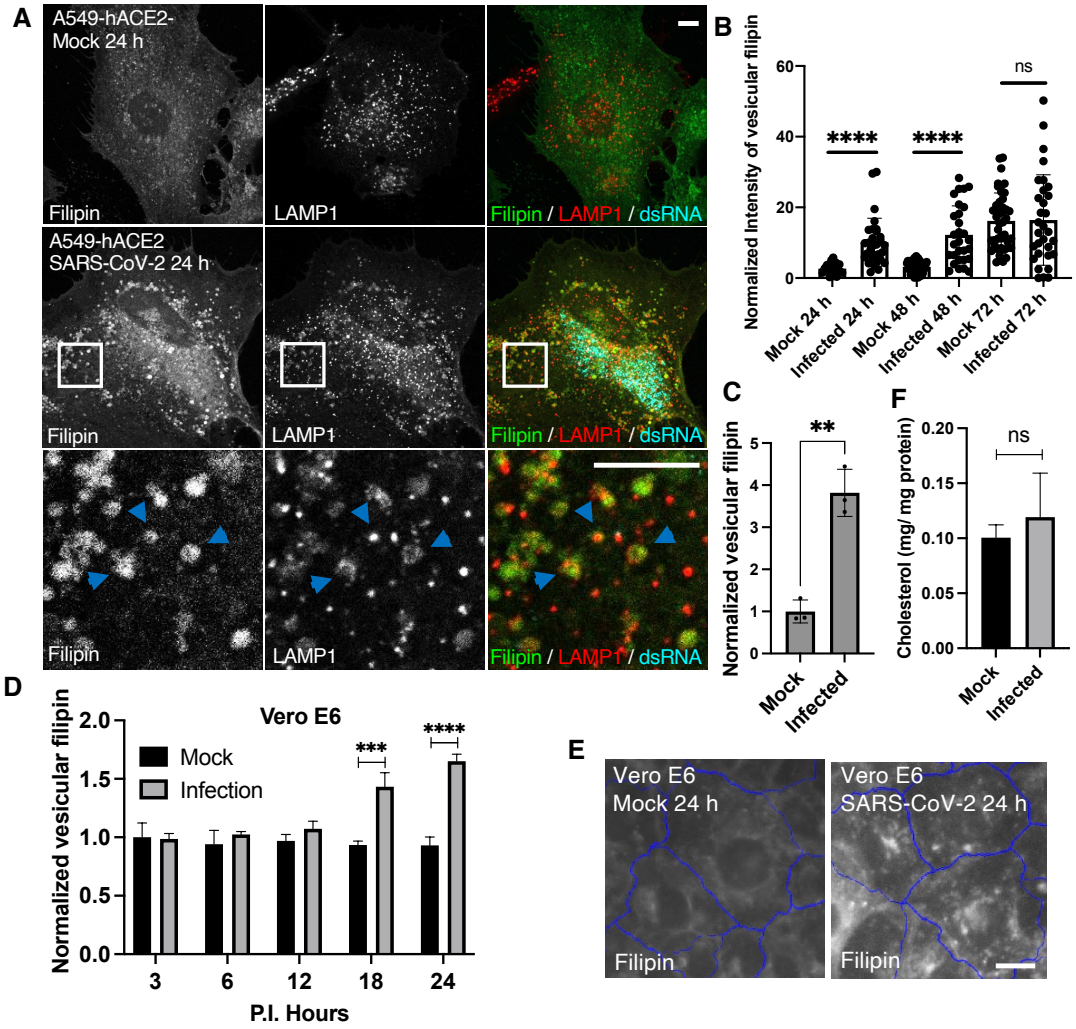

908

909 **Figure 1 Characterization of cellular free cholesterol in SARS-CoV-2 infected cells**

910 **A-C.** A549 cells stably expressing human ACE2 receptor (A549-hACE2) were infected with
911 SARS-CoV-2 and fixed at the indicated time post-infection (P.I.). Filipin was applied to visualize
912 free cholesterol. A dsRNA antibody was used to identify the infected cells. A LAMP1 antibody
913 was used to label lysosomes. Confocal microscopy was performed to collect fluorescence
914 images, and the images at 24 h P.I. were shown in **A**, with arrows pointing colocalized filipin
915 and LAMP1. The intensity of Filipin puncta was quantified with FIJI, and the mean values of
916 total filipin in each cell from three independent experiments were plotted, shown as in **B**.
917 Vesicular filipin was quantified at 24 h P.I. from at least 1,000 infected cells per well and three
918 replicate wells in an experiment by CellInsight microscope platform. Three independent
919 experiments were performed, and pooled results were shown in **C**. **D,E.** Similar experiments

920 were perform as above in Vero E6 cells, and filipin was quantified at the indicated time points.
921 **F.** Total lipids were extracted from mock and infected A549-hACE2 cells at 24 h P.I. and
922 subjected to free cholesterol measurement with GC-MS. Total protein levels were measure by
923 BCA assays. Two independent experiments with 3 replications were performed. Bar graphs are
924 presented as min-max (**B**) or mean ± SD (others). *p* values were determined using *t′* test or One-
925 way ANOVA test. **, $p<0.001$, ***, $p<0.001$, ****, $p<0.0001$, n.s., not significant. Scale bars, 5 μm.

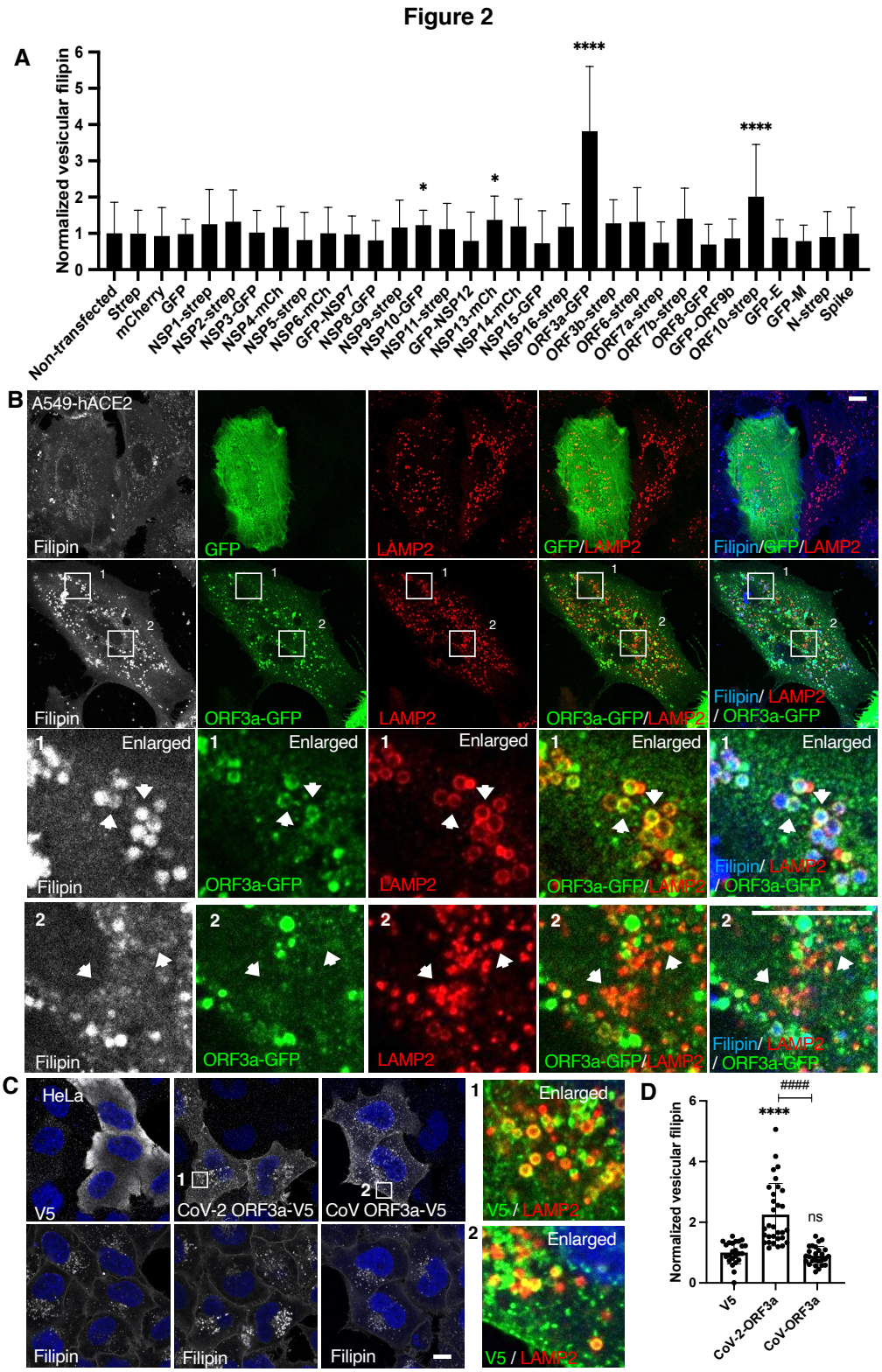

Figure 2 Identification of SARS-CoV-2 proteins responsible for lysosome cholesterol sequestration

929 **A.** Plasmids encoding SARS-CoV-2 proteins were transfected into A549-hACE2 cells
930 individually. Cells were fixed at 24 h post-transfection and co-stained with filipin to visualized
931 free cholesterol and antibodies against the epitope tags to identify transfected cells. Spike
932 protein has no tag and was identified with an antibody. Confocal imaging was performed to
933 randomly take images, and filipin intensity was quantified with FIJI in twenty to fifty cells from
934 two independent experiments. **B.** A549-hACE2 cells were transfected with ORF3a-GFP plasmid
935 as in **A** and co-stained with filipin and GFP and LAMP2 antibodies. **C,D**. HeLa cells were
936 transfected with plasmids encode V5 fused ORF3a proteins in SARS-CoV or SARS-CoV-2. V5
937 alone served as a control. Staining and quantification was performed as described above. Bar
938 graphs are presented as mean ± SD. *p* values were determined using *t'* test or One-way ANOVA
939 test. *, $p<0.05$, **** (vs. control) or #### (CoV vs CoV-2), $p<0.0001$, n.s., not significant. Scale
940 bars, 5 μm. Framed images in C were enlarged 9.36 folds.
941

Figure 3

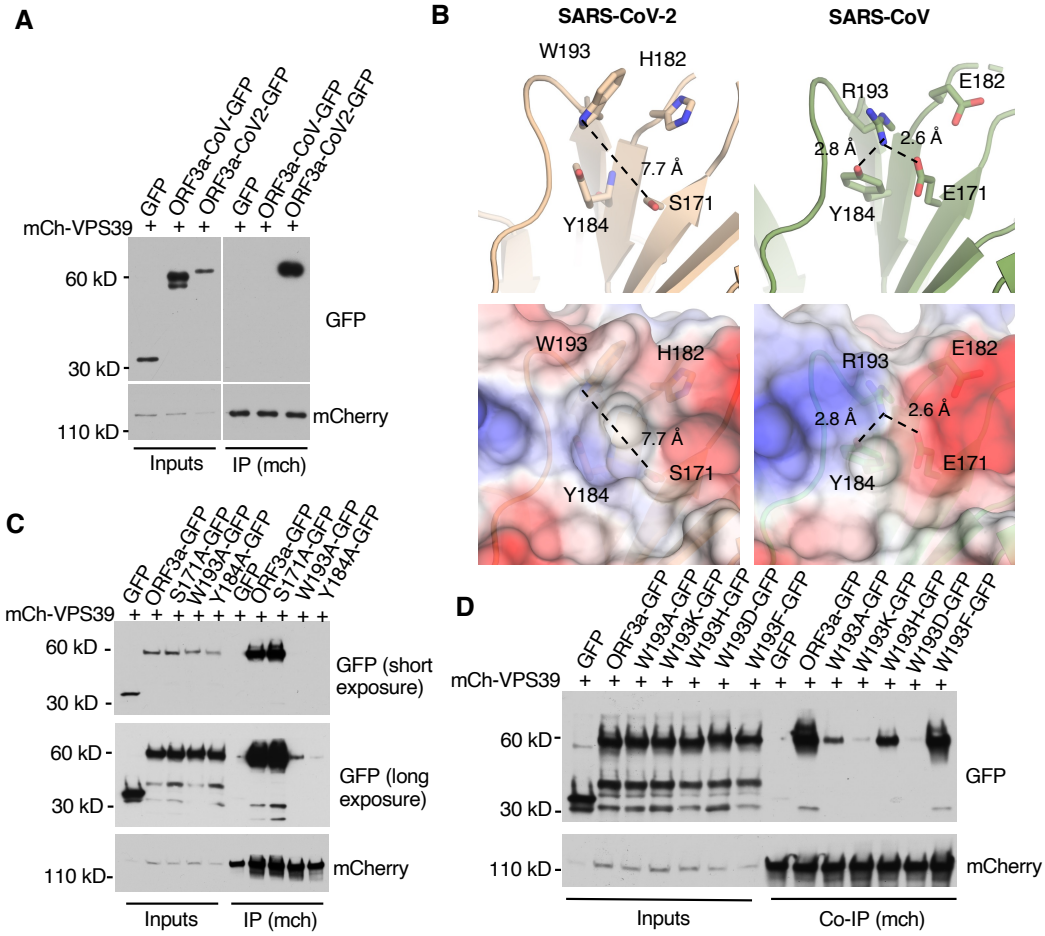

Figure 3 Structural analysis of ORF3a-VPS39 interaction interface in ORF3a

A. HeLa cells were co-transfected with mCh-VPS39 and different GFP-ORF3a constructs as indicated and lysed in a non-denature detergent-contained buffer for co-immunoprecipitation of mCh-VPS39. Immunoblotting was performed to detect GFP signals. **B.** The structures of ORF3a proteins from SARS-CoV-2 (beige) and SARS-CoV (green) were shown with the cartoon representation of the indicated residues (upper panel). The side chains are depicted as sticks with color code for carbon (beige or green), nitrogen (blue), and oxygen (red). The presence of W193 in SARS-CoV-2 induces an open conformation of the divergent loop that is 7.7 Å away from S171 (dotted line), while R193 in SARS-CoV forms hydrogen bonds with D171 or Y184 (dotted lines). The lower panels represent overlays between electrostatics surface and the cartoon representations. Positively charged surface is depicted in blue, hydrophobic surface in white, and negatively charged surface in red. All images and measurements were performed using PyMol V 2.4.0. **C,D.** Transfection and co-immunoprecipitation was performed as

956 described in A to detect the interaction between mCh-VPS39 and GFP-tagged ORF3a and its
957 mutants.
958

Figure 4

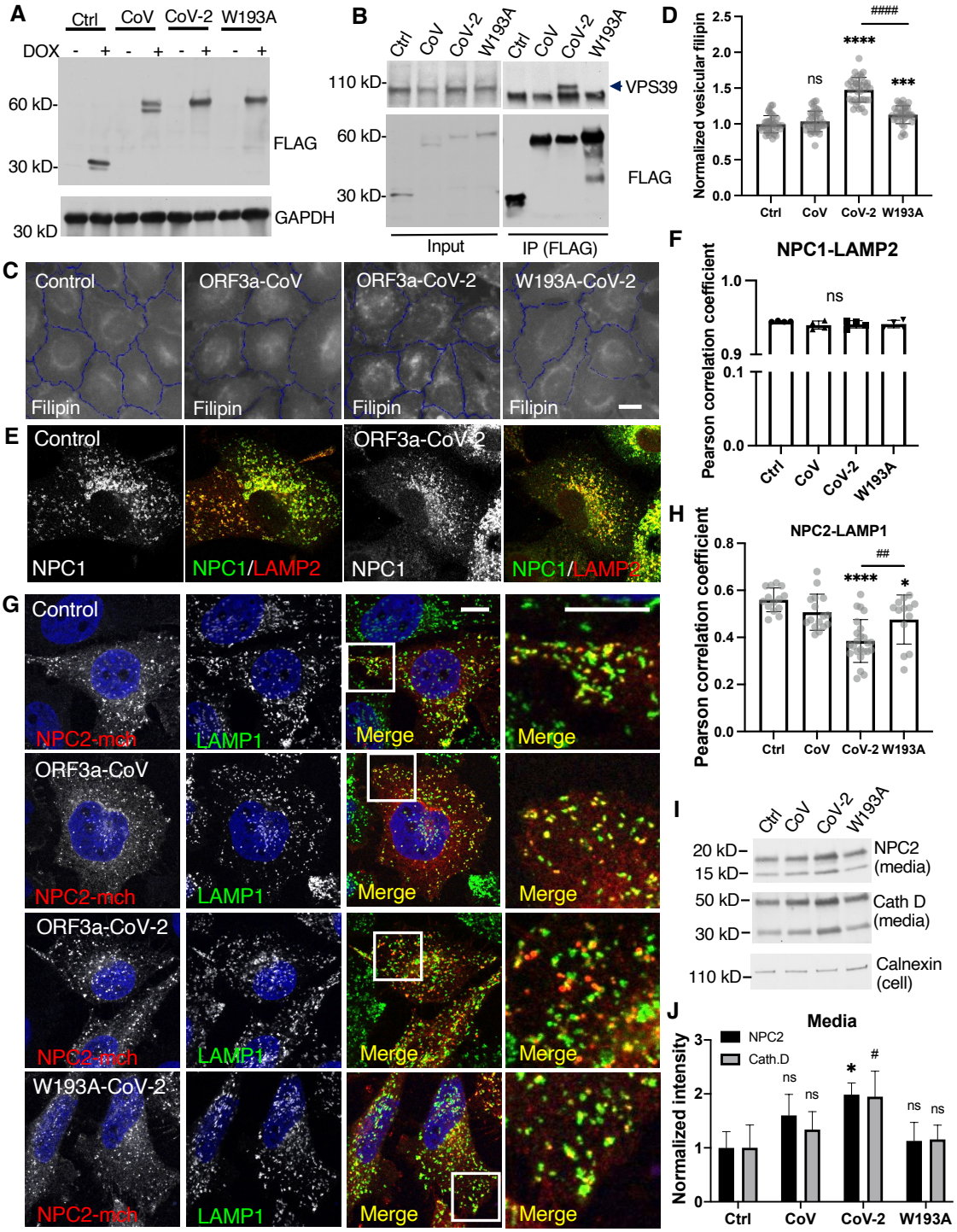

Figure 4 Characterization of NPC proteins in ORF3a-inducible expression cells

A. HeLa-Flp-In cells were established as described in Methods and treated with or without 1 μg/ml doxycycline for 16 hours. Immunoblotting was performed with the indicated antibodies. **B.** Co-immunoprecipitation was performed with FLAG antibody (M2)-coated magnetic beads.

964 Endogenous VPS39 was detected by immunoblotting (arrow). **C,D.** HeLa-Flp-In cells were fixed
965 and stained with filipin, CellMask, and DAPI for high-content imaging. Vesicular filipin was
966 quantified in at least 1,000 cells per well, 6 wells per experiments, 5 independent experiments.
967 **E,F.** Antibodies against NPC1 or LAMP2 were used for immunostaining in fixed cells. Confocal
968 microscopy (**E**) and high-content imaging (**F**) was performed to analyze colocalization between
969 NPC1 and LAMP2. **G,H.** Cells were transfected with NPC2-mCherry plasmid and
970 immunostained with antibodies of mCherry and LAMP1. Confocal microscopy was performed,
971 and FIJI was used to quantify colocalization between NPC2-mCherry and LAMP1 in the cells
972 from two independent experiments. **I,J.** Cell culture media was collected and subjected to
973 immunoblotting using the antibodies indicated. FIJI was used to quantify the bands from 3
974 replications in each of three independent experiments. Bar graphs are presented as mean ± SD. p
975 values were determined using t' test (D,H, CoV-2 vs W193A) or One-way ANOVA test. * or #,
976 $p<0.05$, ** or ##, $p<0.01$, ***, $p<0.001$, **** (vs. control) or #### (CoV-2 vs W193A), $p<0.0001$, n.s.,
977 not significant. Scale bars, 5 μm. Control (Ctrl), linker peptide, CoV, SARS-CoV ORF3a, CoV-2,
978 SARS-CoV-2 ORF3a, W193A, SARS-CoV-2 ORF3a-W193A mutant.

Figure 5

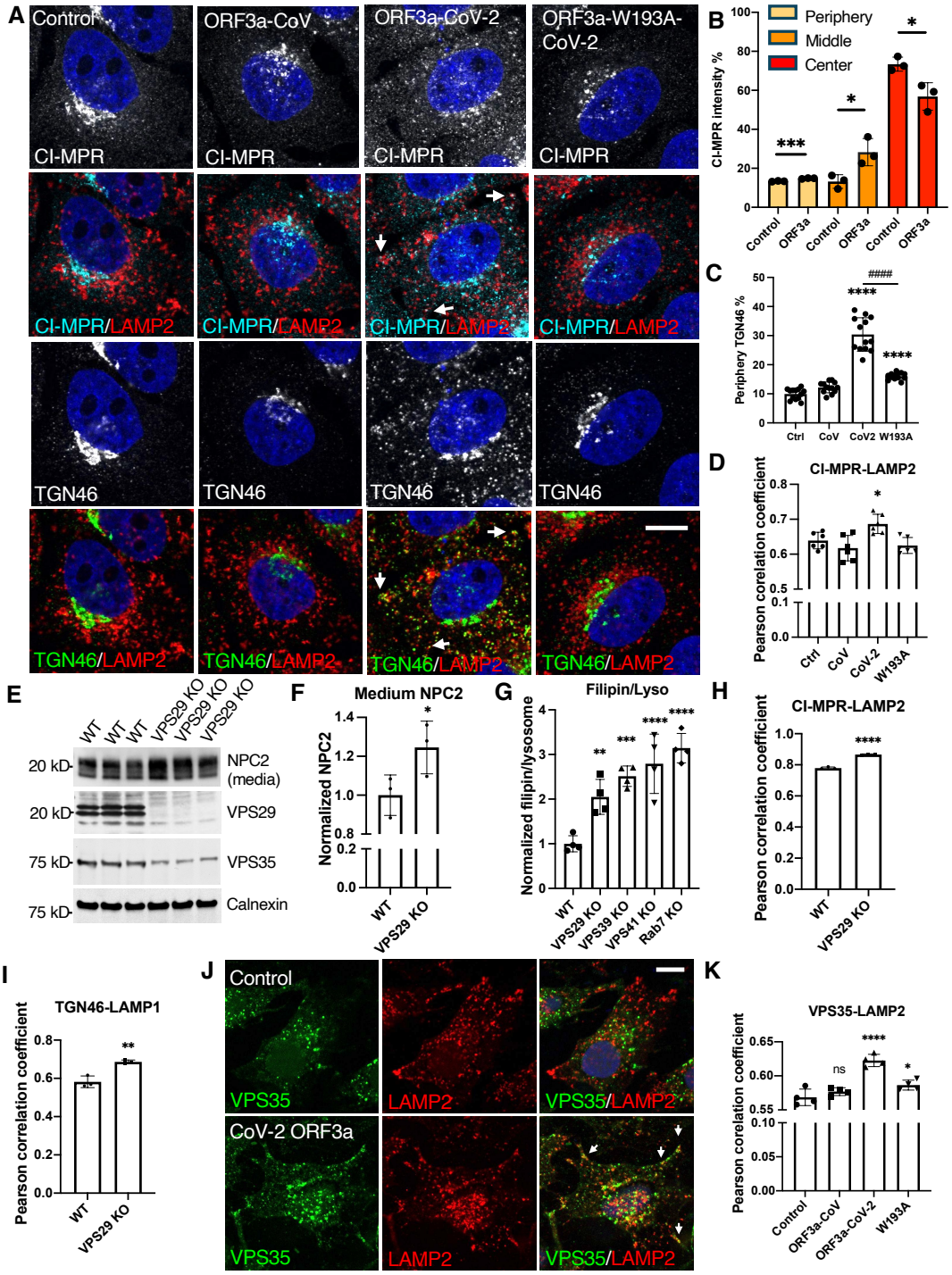

Figure 5 Decreased endosome-to-TGN trafficking

A-D, HeLa Flp-In cells were fixed after 16-h induction of protein expression and immunostained with the indicated antibodies. Confocal microscopy (images) and high-content imaging (bar charts) were performed to analyze protein cellular distribution and colocalization.

984 Periphery was defined as a ring area shrunk from cell boundary with a gap distance 15 pixels
985 (B,C). Center was defined as a dilated circle from nuclear boundary with a distance of 20 pixels
986 (B). Middle was defined as the area between periphery and center (B). **E,F**. Wildtype and
987 VPS29-KO HeLa cell were cultured in serum-free media for 6 hours, and the media were
988 collected before cells were lysed. The media and cell lysates were subjected to immunoblotting
989 with the indicated antibodies. **G**. Vesicular filipin was measured by high-content imaging and
990 normalized to lysosomes in the indicated cells. **H-K,** Cells were fixed and immunostained with
991 the indicated antibodies. Confocal microscopy (images) and high-content imaging (bar charts)
992 was performed to analyze protein colocalization. Bar graphs are presented as mean ± SD. *p*
993 values were determined using *t'* test or One-way ANOVA test *, $p<0.05$, **, $p<0.01$, ***, $p<0.001$,
994 **** (vs. control) or #### (C, CoV-2 vs W193A), $p<0.0001$, n.s., not significant. Scale bars, 5 μm.
995 Control (Ctrl), linker peptide. CoV, SARS-CoV ORF3a. CoV-2, SARS-CoV-2 ORF3a. W193A,
996 SARS-CoV-2 ORF3a-W193A mutant.
997

Figure 6

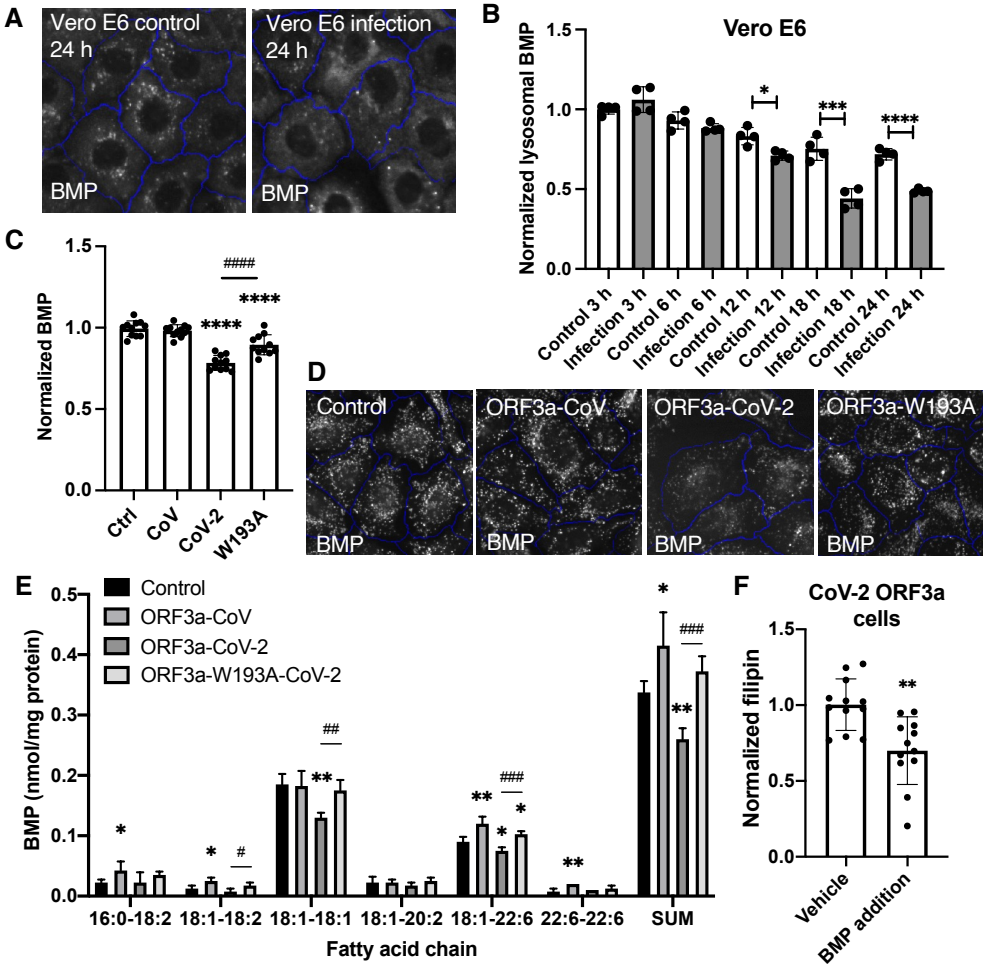

Figure 6 Analysis of BMP levels

A,B. Vero E6 cells were infected with SARS-CoV-2, fixed at the indicated time points post-infection, and immunostained with BMP and LAMP1 antibodies. LAMP1-positive BMP puncta were quantified with the high-content imaging system. Representative images were shown in B. **C,D.** BMP in the HeLa Flp-In cells were measured as described in A. **E.** The indicated cells were harvested and lysed for total lipid extraction. Shotgun lipidomics was performed to identify and quantify bio(monoacylglycero)phosphate (BMP) species based on the fatty acid chains, labeled as carbon number : double-bond number. BMP was normalized to protein concentrations. **F.** Cells were incubated with serum-free media containing 1% BSA and 1 μM BMP for 2 hours, fixed and stained with filipin. filipin levels were measured with high-content imaging. Bar graphs are presented as mean ± SD. p values were determined using t' test or One-way ANOVA test *, p<0.05. **, ##, p<0.01. ***, p<0.001. ****, ####, p<0.0001, n.s., not significant.

1011 Scale bars, 5 μm. Control (Ctrl), linker peptide. CoV, SARS-CoV ORF3a. CoV-2, SARS-CoV-2
1012 ORF3a. W193A, SARS-CoV-2 ORF3a-W193A mutant.
1013

Figure 7

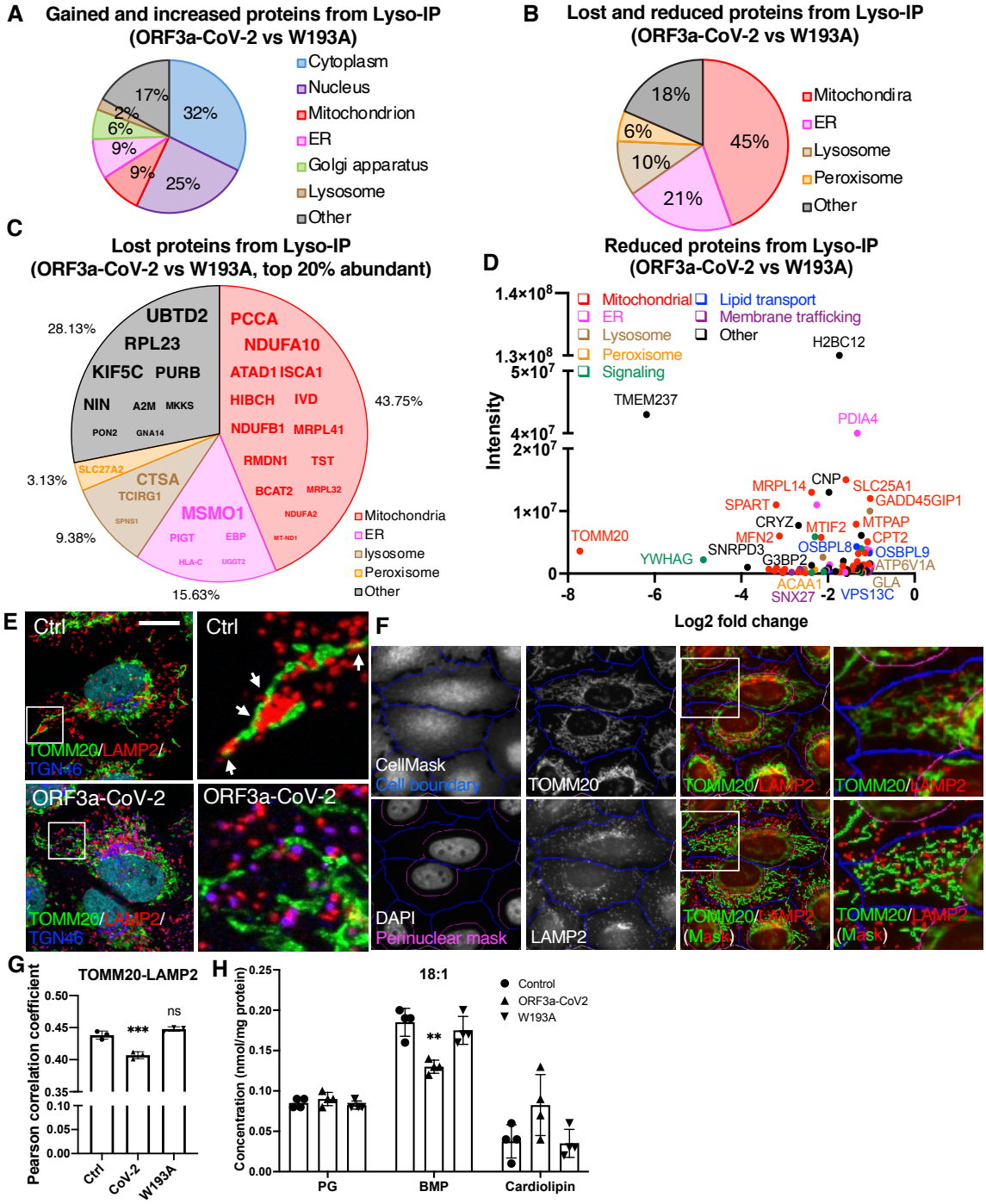

Figure 7. Decreased lysosome-mitochondrion interaction

A-D. Lysosomes were isolated from ORF3a and W193A Flp-In cells, and the total protein were extracted for mass spectrometry analysis. The proteins only presenting in ORF3a lysosomes (gain) or increased more than 2-folds compared to W193A lysosomes (increased) are shown in the pie chart based on their cellular localization (**A**). The proteins only presenting in W193A

1020 lysosomes (lost) or decreased more than 50% compared to W193A (reduced) are shown in **B.**
1021 Amount the lost proteins, as defined above, top 20% abundant proteins in W193A lysosomes
1022 are shown in **C.** The reduced proteins, as defined above, were plotted in **D**. The color codes
1023 reflect their cellular localization or functions. **E**. The control and CoV-2 ORF3a cells were fixed
1024 and immunostained with the indicated antibodies. Confocal microscopy was applied for
1025 imaging. Arrows indicate the lysosome-mitochondrion physical interactions. Scale bar, 5 μm.
1026 **F,G.** The Flp-In cells were fixed and immunostained with the indicated antibodies accompanied
1027 with CellMask and DAPI. High-content imaging system was used for image collection and
1028 analysis. Cell boundary and perinuclear area were defined based on CellMask and DAPI,
1029 respectively. Lysosome and mitochondrial masks were defined with LAMP2 and TOMM20
1030 signals, respectively. The colocalization between lysosomes and mitochondria were quantified
1031 and presented as Pearson correlation coefficient. **H.** Total lipids were extracted from the
1032 indicated cells and subjected to shotgun lipidomics analysis. PG, BMP, and Cardiolipin with the
1033 18:1 fatty acid chains are presented. PG, phosphatidylglycerol. BMP,
1034 bis(monoacylglycerol)phosphate. Bar graphs are presented as mean ± SD. *p* values were
1035 determined using One-way ANOVA test **, $p<0.01$. ***, $p<0.001$. n.s., not significant.
1036

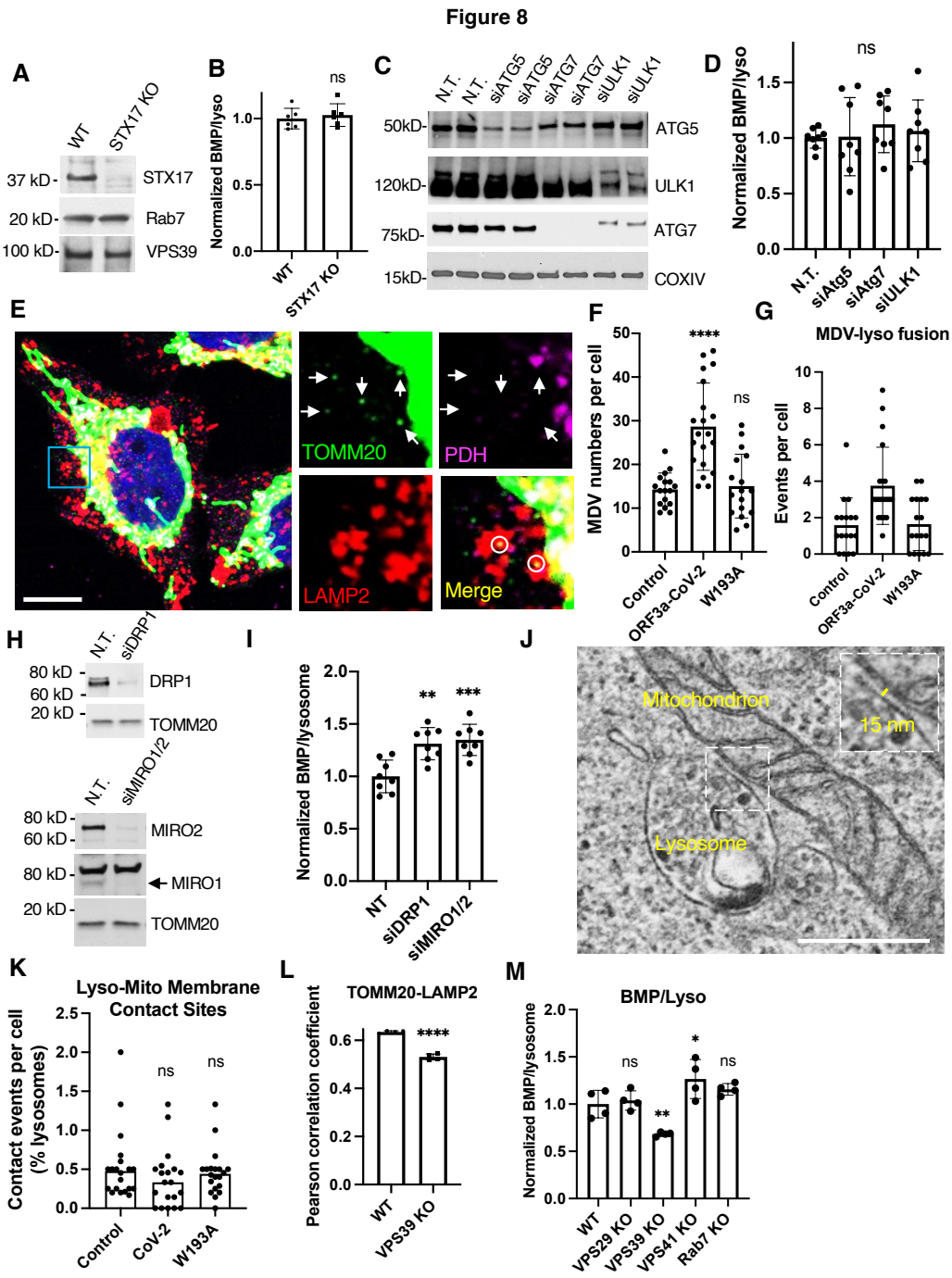

Figure 8. Involvement of impaired lysosome-mitochondrion membrane contact sites in BMP reduction

A.B, Wildtype and STX17-knockout (KO) HeLa cells were lysed for immnoblotting with the indicated antibodies (**A**) or fixed for immunostaining and hign-content imaging quantification (**B**). **C.D,** Wildtype HeLa cells were transfected with siRNA targeting the indicated autophagy genes. Non-targeting siRNA (N.T.) served as a control. Protein levels were examined by immunoblotting (**C**), and the BMP levels were measured by immunostaining followed by high-

1045 content imaging (**D**) at 2 days post-transfection. **E-G,** The Flp-In cells were fixed and
1046 immunostained with a TOMM20 (marker of mitochondrion-derived vesicles, MDVs), PDH
1047 (maker of mitochondria but not MDVs), and LAMP2 (lysosome marker) antibodies. Confocal
1048 microscopy was performed to identify MDVs (arrows) and the MDVs fused with lysosomes
1049 (circles) (**E**). The MDV numbers (**F**) and the number of lysosome-fused MDVs (**G**) were
1050 quantified using FIJI. Scale bar, 5 μm. **H.I,** HeLa cells were transfected with the siRNAs of N.T.,
1051 DRP1, or combined MIRO1 and MIRO2 and subjected to immunoblotting (**H**) or high-content
1052 imaging quantification (**I**). **J.K,** The Flp-In cells were seeded on glass coverslips, fixed, and
1053 subjected to electron microscopy. Randomized cells were imaged at mitochondrion-existing
1054 areas. Lysosome-mitochondrion membrane contact sites were identified by their membrane
1055 structures and the distance between membranes (**J**) and quantified from 20 cells of each type
1056 (**K**). Scale bar, 0.5 μm. **L.M,** Wildtype and VPS39-knockout (KO) HeLa cells were
1057 immunostained and subjected to high-content imaging quantification. Bar graphs are presented
1058 as mean ± SD. p values were determined using t' test or One-way ANOVA test. *, $p<0.05$. **,
1059 $p<0.01$. ***, $p<0.001$. ****, $p<0.0001$. n.s., not significant.